

Università degli Studi di Genova
Scuola di Scienze Matematiche, Fisiche e Naturali

Anno Accademico 2024/2025

Tesi di Laurea Magistrale in Fisica
Curriculum di Fisica delle Interazioni Fondamentali

Opening Pandora's box
A dedicated study of the automatic event
reconstruction in the ICARUS-T600
experiment

Candidato
Mattia Sotgia

Relatrice
Dr. Alice Campani
Relatore
Prof. Marco Pallavicini

Correlatrice
Carla Biggio

Genova, 15 ottobre 2025

I have done something very bad today by
proposing a particle that cannot be
detected; it is something no theorist
should ever do.

(Wolfgang Pauli)

Abstract

The three-flavor neutrino mixing minimal extension of the Standard Model (SM) has been established by a number of experiments in the past two decades. However, a series of experimental anomalies were observed, indicating a possible hint of the existence of a fourth neutrino, called *sterile neutrino* because it does not undergo weak interaction.

This $3 + 1$ extension of the SM is the main physics target of the ICARUS experiment as part of the Short-Baseline Neutrino (SBN) program at Fermilab. The ICARUS-T600 760-ton detector is a Liquid Argon Time Projection Chamber (LAr-TPC) successfully employed at the LNGS laboratories for a three-year physics run and now collecting data at Fermi National Accelerator Laboratory (FNAL). The physics program of the ICARUS experiment also includes the measurement of neutrino-Argon cross sections employing the off-axis Neutrino at the Main Injector (NuMI) beam and several Beyond Standard Model studies.

The automatic TPC event reconstruction in ICARUS is performed using the Pandora Pattern Finding Algorithm framework that performs a 3D reconstruction of the image recorded in the collected event, including the identification of interaction vertices and the classification of tracks and showers inside the TPC.

In view of the standalone ICARUS oscillation ν_μ CC analysis and of the future combined SBN oscillation analysis, a thorough evaluation of the performances of reconstruction chain, as well as the systematic uncertainties induced on the reconstructed neutrino energy spectrum is essential. The main objective of this work is to evaluate the performances of single steps of the reconstruction sequence, while possibly testing improvements of the machine learning algorithms employed in specific stages of the chain.

Acknowledgement

Mattia
15 ottobre 2025

Contents

Introduction,	1
Chapter 1	Active and sterile neutrinos, 5
1.1	Neutrinos, an history journey, 5
1.2	Neutrinos in the Standard Model, 7
1.2.1	Neutrino interactions, 7
1.2.2	Flavour oscillations, 11
1.3	Short baseline anomalies, 22
1.3.1	The sterile neutrino hypothesis, 26
1.3.2	Experimental status and future perspectives, 27
Chapter 2	The SBN program at Fermilab and the ICARUS experiment, 33
2.1	The Short Baseline Neutrino program at Fermilab, 33
2.1.1	Neutrino beam, 37
2.2	Liquid Argon Time Projection Chambers, 39
2.3	The SBN near detector: SBND, 43
2.4	The ICARUS-T600 detector, 44
2.4.1	The ICARUS subsystems, 48
Chapter 3	ICARUS-T600 detector operations and event reconstruction, 51
3.1	Data acquisition, 51
3.2	ICARUS data processing, 54
3.3	Light reconstruction, 55
3.4	Wireplanes signal reconstruction, 56
3.5	Cosmic ray tagger reconstruction, 59
Bibliography,	63

List of Figures

1.1	(Anti)Neutrino-matter cross-sections	9
1.2	Diagrams of some interaction topologies for neutrinos in matter	10
1.3	The solar neutrino flux produced by all the reactions inside Sun's core	13
1.4	SNO+SK results for the “solar neutrino problem”	15
1.5	Neutrino mass ordering	19
1.6	The LNSD detector and results	24
1.7	MiniBooNE detector and results	25
1.8	Neutrino mass ordering with the sterile state	27
1.9	Parameter spaces in both the ν_e appearance and ν_μ disappearance channels	30
1.10	Status of the global experimental searches	31
2.1	Electron neutrino appearance probability in the 3 + 1 sterile oscillation scenario	34
2.2	SBN sensitivity plots in both appearance and disappearance channels .	36
2.3	Fermilab Accelerator complex	37
2.4	BNB flux predictions at the near and far detectors	38
2.5	LArTPC illustration	40
2.6	T300 module Induction-2 and collection planes wire orientation	45
2.7	ICARUS TPC wires and field cage	46
2.8	ICARUS detector illustration	47
2.9	BNB and NuMI collected POT	48
3.1	ICARUS DAQ illustration	53
3.2	<i>Stage0</i> and <i>Stage1</i> data processing pipeline	55
3.3	PMT reconstructed <i>OpHits</i>	56
3.4	TPC plane signal	57
3.5	TPC signal processing	58
3.6	CRT Hit reconstruction in space	60

Introduction

Neutrinos are the most abundant particle in the universe, with billions of neutrinos passing through each square centimetre each second, primarily coming from our neighbour star, the Sun: within nuclear reactions inside the Sun's core, billions of neutrinos are created, and, due to their weakly interactive nature, they travel unaltered to Earth. Other neutrino sources are also core-collapse supernovae, interacting cosmic rays within Earth's atmosphere, and, nonetheless, nuclear reactors and accelerator complexes.

The discovery of neutrino oscillations, hence the evidence for neutrino masses, is a striking proof of Beyond the Standard Model (BSM) physics. Generating neutrino masses is qualitatively different from generating masses for any other fermionic particle content of the Standard Model (SM). Several are the possible scenarios for introducing neutrino masses in the SM: in general, the mechanism of neutrino masses would require the addition of new particle states to the SM that have never been observed. The addition of these particle states would modify substantially neutrino-related observables and would have effects, for example, on oscillation phenomenology.

Interest in this direction has been fanned, more recently, by a series of anomalous neutrino measurements at short-baseline oscillation experiments at accelerating complexes, like the LSND and MiniBooNE collaborations; at Gallium-based experiments, like GALLEX, SAGE and BEST collaborations; and at reactor baselines, like the Neutrino-4 collaboration.

None of these short-baseline experimental anomalies, however, proved to be definitive, even if the global picture shows a strong tension with the current model. An individual program aiming at a $> 5\sigma$ sensitivity, on multiple short-baseline oscillation channels experiment is needed to test these results and draw a complete picture for these short-baseline experimental anomalies.

The Short Baseline Neutrino (SBN) program at Fermilab is a three-detector, short-baseline, multiple-oscillation-channel experimental effort located along the Booster Neutrino Beam (BNB) baseline. All three detectors in the beamline are Liquid Ar-

2 Introduction

gon Time Projection Chambers (LArTPC(s)), exploiting the high precision calorimetric power and mm-scale three-dimensional tracking capabilities of such detectors to achieve unprecedented sensitivity on the sterile neutrino search.

The ICARUS T600 detector acts as the SBN Far Detector (SBN-FD) at a baseline of 600 m. The location of both the ICARUS detector and of the SBN Near Detector, SBND, was chosen to optimise neutrino oscillation sensitivity and minimise the impact of flux systematics. Among the Booster Neutrino Beam, the ICARUS T600 detector is also on the baseline of the Neutrino from the Main Injector (NuMI) Beam, crossing the detector 6° off-axis with respect to the detector principal axis. The ICARUS detector has now finished its fourth physics campaign, three of which were done while the SBN near detector was preparing to start its physics operation. With all this data the collaboration has started to look into ν_μ -disappearance studies, with the simplest topologies being $1\mu 1p$ and $1\mu Np$.

In order to reduce the systematic uncertainties related to the reconstruction efficiency, a detailed study of the event reconstruction inside the ICARUS TPC is needed, alongside an effort to align the ICARUS and SBND detectors signal processing and event reconstruction chain, in view of the future SBN joint analysis.

Of all steps involved in the event processing and reconstruction, one of great importance is related to the particle objects building from the signals left on the wire-planes and the subsequent event hierarchy creation (that is, defining which are the primary particles originating from the interaction vertex and the interaction *structure*), which is the centrepiece of many further analyses. This process is performed by a set of algorithms shared across the LArTPC technology detectors. The common framework is based on the Pandora Patter Finding Algorithm software. This features, alongside the various algorithms suited for the reconstruction, a set of tools that can be used to perform studies on the reconstruction efficiency, previously unused by the ICARUS collaboration.

The aim of this thesis is twofold: first, to validate this set of tools for further use in the ICARUS collaboration, and second, to demonstrate their effectiveness by conducting a thorough efficiency analysis of the TPC reconstruction chain. This will serve as validation for the current analysis and lay the groundwork for future work, such as the future ν_e -appearance analysis, where these tools can be used to validate the reconstruction of shower-like particles. The reconstruction of these particles is difficult due to the topology of the particle-argon interaction and the signal it produces.

The thesis structure is as follows

- [chapter 1](#) is devoted to introducing the theoretical framework of the Standard Model of Particle Physics, with a great interest on the physics of neutrinos,

their *classical* picture, the phenomenology of neutrino oscillator behaviour, and some of the anomalies driving the sterile neutrino picture.

- [chapter 2](#) tries to get a detailed description of the ICARUS T600 detector, its three sub-systems (the Liquid Argon Time Projection Chamber, the light collection system, and the cosmic ray tagging system), and its role in the Fermilab Short Baseline Neutrino Program.
- [chapter 3](#) is dedicated to an overview of the complete chain the collected data follows, from when it is acquired by the DAQ system to the processing stages allowing this data to be informative. It focuses on how signals from all sub-detectors is reconstructed, with a primary focus on the TPC event reconstruction.
- ?? ...
- ?? ...

1

Active and sterile neutrinos

It doesn't matter how beautiful your theory is, it doesn't matter how smart you are. If it doesn't agree with experiment, it's wrong.

(Richard P. Feynman)

1.1 Neutrinos, an history journey

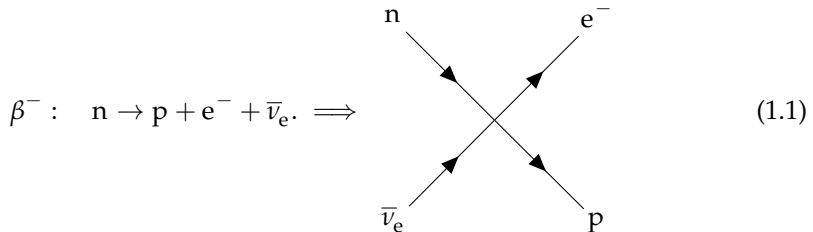
Dating back to 1914, the history of neutrinos began with the first paper published by Sir James Chadwick [1], who, investigating the phenomena of beta decays, discovered that the emitted electron energy spectra was not a single vertical emission line (delta shaped) but a continuous spectrum.

The β decay process, up until then, was thought to be just the emission of a single electron from a neutron decaying at rest to a proton, $n \rightarrow p + e^-$, and so it was expected the electron to carry all the neutron energy. A continuous e^- spectrum broke this expectation. W. Pauli in 1930 proposed the idea that the emission of the electron occurred along with the emission of another fermionic particle, far less massive — massless even — than the electron, carrying no electric charge [2] $n \rightarrow p + e^- + \bar{\nu}_e$. Though not calling this particle “neutrino” yet, its idea was all contained in Pauli’s letter.

Enrico Fermi, a prominent scientist of that era, developed Pauli’s idea, calling this new particle *neutrino* [3, 4] — from *neutron*, the only chargeless particle discovered so far, aside from photons — adding the suffix *-ino*, meaning smaller (and lighter). Fermi’s idea was the first *field theory* of quantum mechanics, suggesting that the β decay was to be formalized as a four-fermion point interaction, involving a neutron

6 Chapter 1 Active and sterile neutrinos

decaying to a proton to produce an electron and a neutrino,



Fermi's effective theory was able to explain the β decay energy spectrum of the electron successfully, even preserving the angular momentum conservation. The value of the coupling measured by Fermi for this interaction, called G_F , was

$$G_F^{(\beta)} \simeq 1.166 \times 10^{-5} / \text{GeV}^2, \quad (1.2)$$

implying that this type of interaction was minimal, which justified calling this type of interaction *weak*. Up until now, however, the neutrino was yet to be "directly" observed. It took twenty-six years of experimental efforts to actually detect the traces of this "ghostly" particle. The first experimental observation of electron antineutrinos produced by beta decays from the Savannah River reactor happened in 1956; a team led by F. Reines and C. L. Cowan observed the signature of inverse beta decay process (IB)

$$\bar{\nu}_e + p \rightarrow n + e^+ \quad (1.3)$$

in a water tank, detecting the two gamma rays from proton annihilation in water with a liquid scintillator [5].

The world of particle physics was discovering new particles very fast and putting together the picture we today know as the Standard Model (SM) of particle physics: in the same years the electron neutrino was discovered, a team led by Carl D. Anderson and Seth Neddermeyer was discovering the muon by looking at charged particles in the atmosphere, which they described as a heavier relative to the electron, since it showed a less prominent curvature than the electron when passed through a magnetic field; this discovery was later confirmed [6–8]. The discovery of the muon led to many starting to question about the relationship that neutrinos had with muons and electron. In 1959 Bruno Pontecorvo examined this problem and questioned himself the nature of neutrinos [9]: are neutrinos produced alongside electrons and neutrinos produced alongside muons the same?. This led to the neutrino experiment at Brookhaven National Laboratories (BNL) guided by L. M. Lederman, M. Schwarz, and J. Steinberger. At BNL, using the Brookhaven Alternating Gradient Synchrotron (AGS), protons were accelerated toward a beryllium

target: the resulting kaons and pions decayed in-flight, producing muons and muon antineutrinos. Using a spark chamber located behind a concrete wall stopping the produced muons, they were able to detect the muon produced by the interaction of muon antineutrinos but saw no electron-like event. This constituted a valid proof that there are at least two *families* of neutrinos.

In 1989 the ALEPH detector at the LEP e^+e^- collider studied the Z^0 resonance and set strong constraints on the number of neutrino families $N_\nu \simeq 3$ [10], ruling out the possibility of a fourth (active) neutrino family and still suggesting a third — up until then unobserved — neutrino should exist. In 1975 the third “*heavier*” brother of the electron and the muon, the tau, was discovered [11]; this discovery led physicists to expect that a third neutrino had to exist. The tau neutrino signature was finally detected in 2000 in the DONuT (Direct Observation of the Nu Tau) experiment at Fermilab, twenty-five years after the discovery of the tau lepton.

1.2 Neutrinos in the Standard Model

The state of the art of particle physics is defined by the Standard Model (SM). In the SM of particle physics the strong, weak and electromagnetic interactions are described by the gauge symmetries $SU(3)_C \times SU(2)_L \times U(1)_Y$ [12]. The SM is the most comprehensive theory of particle physics, and has been experimentally tested with high accuracy. Neutrinos in the SM are massless fermions — meaning that their spin is half-integer — that do not have strong nor electromagnetic interactions. As all the particles in the SM, we can define the helicity $\mathcal{H} = \sigma \cdot \mathbf{p}/|\mathbf{p}|$ as the projection of the spin σ on the particle momentum \mathbf{p} ; however, differently to other particle content of the SM, for neutrinos only left-handed ($\mathcal{H} = -1$) neutrinos and right-handed ($\mathcal{H} = +1$) neutrinos have been observed. The experimental evidence of this peculiarity of neutrinos was discovered by M. Goldhaber, L. Grodzins and A. W. Sunyar in 1958 [13]. Helicity for massless particles is equivalent to their chirality (or handedness), which is why we can define positive helicity as right-handed and negative helicity as left-handed.

The standard model for particle physics account for three families of neutrinos, each paired with the corresponding charged lepton: the electron neutrino ν_e , the muon neutrino ν_μ and the tau neutrino ν_τ .

1.2.1 Neutrino interactions

In the SM neutrino can, therefore, only interact via the weak interaction, which is mediated by three vector bosons (vector since they have integer spin), W^\pm and Z^0 .

The experimental evidence of the W^\pm and Z^0 bosons, constituting a strong proof of the SM theory, arrived between 1982 and 1983. The experiments UA1/UA2, led by Nobel physics laureate Carlo Rubbia, placed inside the CERN-Sp \bar{p} S accelerator ring, saw signatures of these bosons with proton-antiproton collisions with a high significance [14, 15].

The type of interactions that are possible for neutrinos are multiple. Giving a general enough picture of such interaction, usually a neutrino can create a vertex with either a W boson — thus resulting in a charged current (CC) event, with the corresponding charged lepton on the other side of such vertices — or with a Z boson — resulting in a neutral current (NC) interaction, where the outgoing particle is the same flavour neutrino. In both cases, the diagram is completed by stitching on the other side of the boson line the interaction with the matter. The interaction in its entirety is required to conserve both charge and momentum. According to what the final state particles of the interaction are, the interactions themselves can be classified.

Charged current interactions Neutrino-matter interactions show a rich phenomenology that varies dramatically across different energy scales. Multiple mechanisms determine the total cross-section of the ν -matter interaction, as shown by Figure 1.1.

- Starting on the lower part of the energy spectrum, the first mechanism is the quasielastic interaction. These have an energy peak around $E_\nu \simeq \mathcal{O}(1\text{ GeV})$. In a QE event, the neutrino scatters off an entire nucleon rather than its constituent partons, converting the neutron to a proton and emitting a charged lepton

$$\nu_\ell + n \rightarrow \ell^- + p, \quad \bar{\nu}_\ell + p \rightarrow \ell^+ + n. \quad (1.4)$$

The diagrams corresponding to such processes are shown in Figure 1.2a. The QE neutrino cross-section can be accurately described by the V-A interaction theory, which is an intermediate description between the Fermi four-point interaction and the SM [16].

- As we approach $E_\nu \simeq \mathcal{O}(10\text{ GeV})$, the neutrino can excite the struck nucleon to an excited state. In this case, the neutrino interaction produces a baryon resonance, which quickly decays to a nucleon and single pion final state, as illustrated in figure 1.2c

$$\nu_\ell + p \xrightarrow{\Delta^{++}} \ell^- + \pi^+ + p \quad (1.5)$$

In such resonance productions, the neutrino interaction can be coherent, meaning the neutrino coherently scatters from the entire nucleus. These are referred

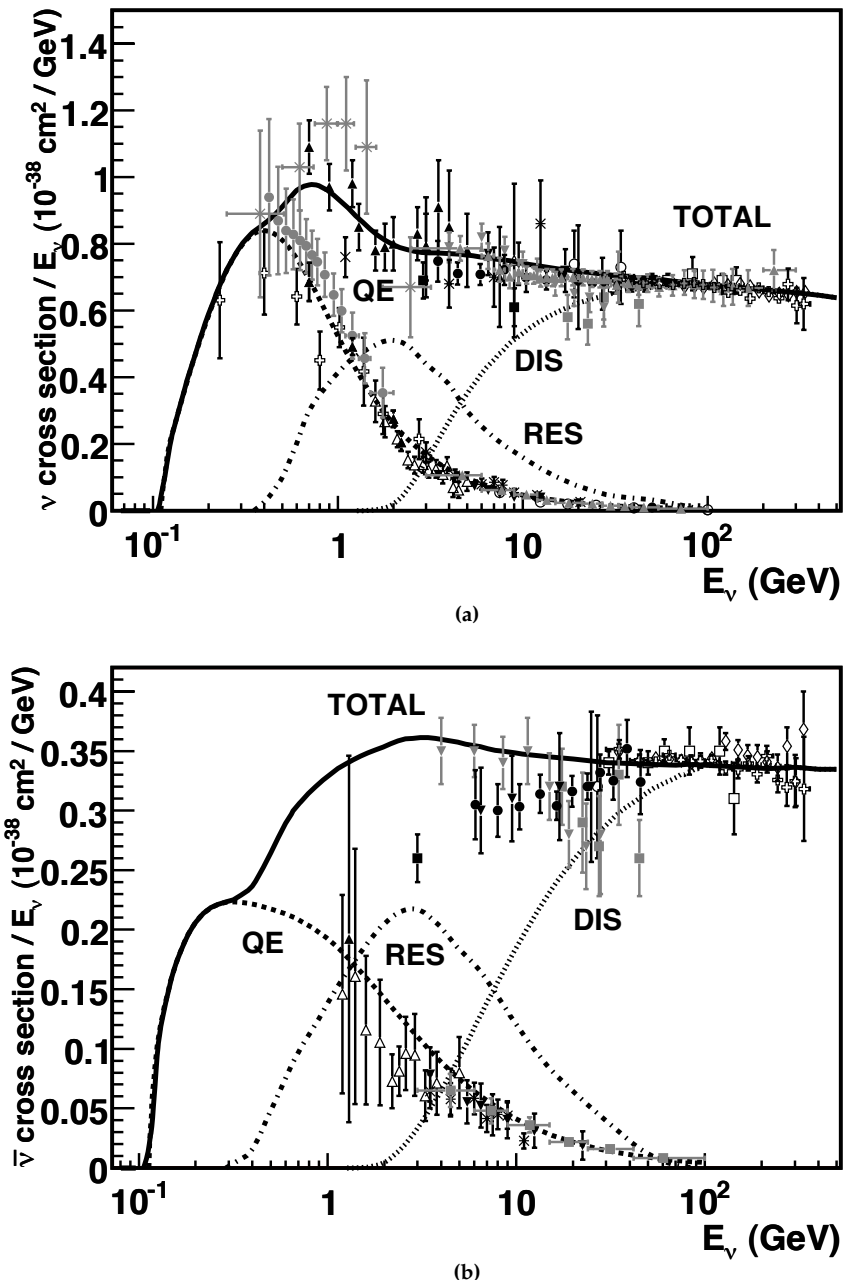


Figure 1.1 Cross-section measurements for (anti)neutrino-nucleon charged current interactions, showing the contributions of quasi-elastic, resonant, and deep-inelastic-scattering processes, both for neutrinos (a) and for antineutrinos (b). Figures adapted from Ref. [16].

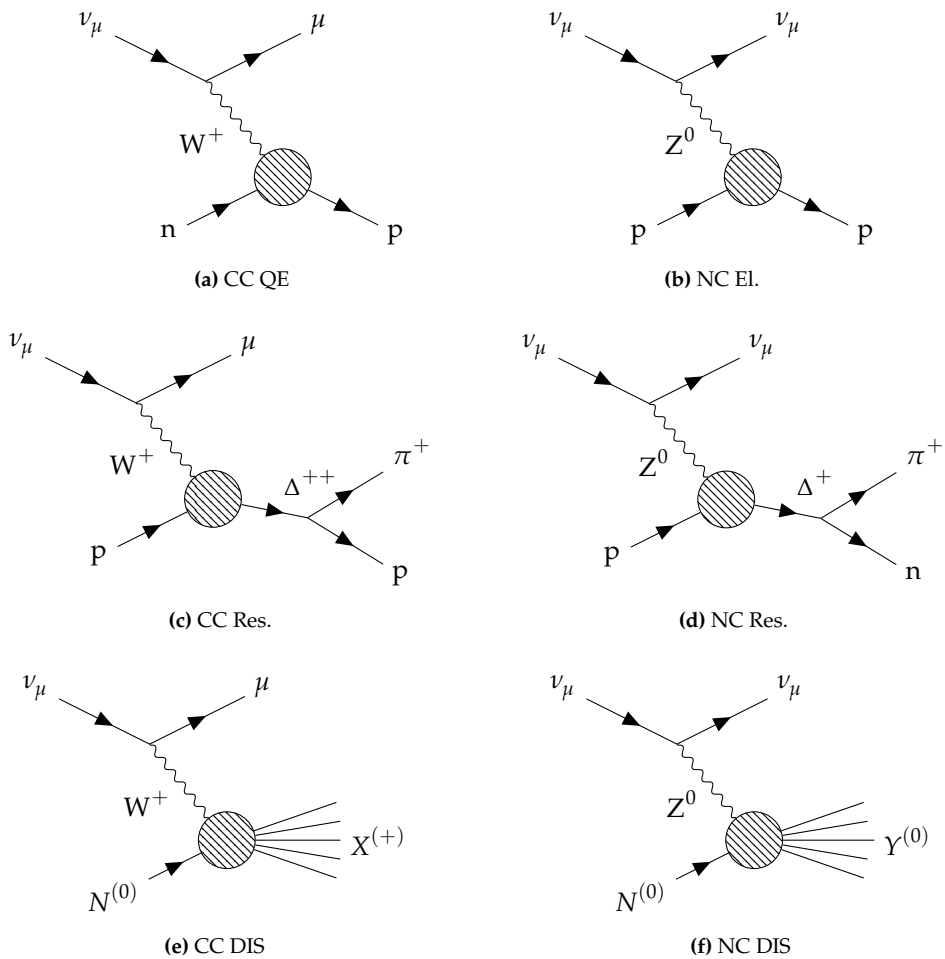


Figure 1.2 Diagrams of some interaction topologies for neutrinos in matter

to as coherent single pion final states, and such interactions have a small transferred momentum to the nucleon, producing no nuclear recoil and a distinctly forward-scattered pion.

- When the neutrino energy exceeds 10 GeV, the interaction is entirely at the parton level, breaking the nucleons and producing a final state interaction with high multiplicity,

$$\nu_\ell + N^{(0)} \rightarrow \ell^- + X^{(+)}, \quad \bar{\nu}_\ell + N^{(0)} \rightarrow \ell^+ + X^{(-)} \quad (1.6)$$

where $X^{(\pm)}$ indicates the ensemble of the final state particles, with this notation highlighting that charge is still conserved, so an overall positive charge

is expected. This interaction is called Deep Inelastic Scattering (DIS). This is exemplified in Figure 1.2e.

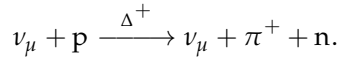
Neutral current interactions Up to this point, I presented only the charged current interactions topologies for neutrinos. Of course, as previously anticipated, the possible interactions include neutral current topologies that present the exchange of a Z^0 boson. Looking at the classification for CC events, we also have a similar classification for NC topologies.

- The lower part of the energy spectrum is populated by elastic scattering of neutrinos on nucleons, with each particle involved in the process not changing its nature,

$$\bar{\nu}_\ell^{(-)} + N \rightarrow \ell^\pm + N, \quad \text{with } N = p, n.$$

One of these processes is presented in Figure 1.2b.

- NC Res. and NC Coh. single pion scattering processes are also possible, with a plethora of events possible; in Figure 1.2d there is the single pion process mediated by the Δ^+ baryon



- Finally, at high energy, the NC DIS processes are possible. Figure 1.2f shows an illustration of a DIS process, $\nu_\mu + N^{(0)} \rightarrow \nu_\mu + Y^{(0)}$.

The Gargamelle experiment [17] was a central experiment in the history of neutrino physics, being the first to actively detect signatures of neutral weak current events, thus confirming the validity of the weak interaction model [18, 19]. Full reviews of the neutrino interactions in matter (expanding more on the processes displayed in Figure 1.2) are found in Ref. [16, 20]

1.2.2 Flavour oscillations

Neutrinos are one of the most abundant “visible” particles in the universe. They are produced in multiple channels, many *natural*, some *artificial*. The production mechanism is correlated with the energy of the neutrinos.

- Neutrinos in the MeV scale are generated in reactions inside the stars cores (such as the Sun) through the pp-chain and the CNO cycle reactions;
- On the artificial side, neutrinos in the MeV region are those coming from nuclear fission reactors: electron antineutrinos originate as the β -decay products

from unstable decaying fissioning isotopes such as ^{238}U and ^{239}Pu . The energies peak at 3 MeV and extend up to 8 MeV;

- The core part of the energy spectrum, from some GeV to some TeV, is composed of atmospheric neutrinos, coming from cosmic rays interacting within the atmosphere. Those also compose the highest part of the spectrum;
- In the core region, there are also accelerator-borne beams of neutrinos. Those extend from some hundreds of MeV to some tens of GeV. These constitute an interesting part of the spectrum since their power can be controlled, hence their flux, making it easier to study in greater detail the properties of neutrinos.

Up to this point, the description of neutrinos has been of massless neutral leptons. However, experimental observations suggested otherwise.

Dating back to the discovery of neutral mesons, the idea of flavour oscillation was established for massive particles. This was the case for the $\text{K}^0/\bar{\text{K}}^0$ oscillation discovery, which was studied to get an explanation for the regeneration of short-lived neutral kaons, K_S^0 [21]. This type of oscillatory behaviour is well explained by the weak interaction of quarks in the SM Lagrangian with the Higgs mechanism that gives masses to quarks themselves, hence to mesons. Therefore, oscillatory behaviour is explained by the particle having mass.

For neutrinos, such a hypothesis did not hold true, and so no flavour oscillation was expected. However, theoretical models of neutrino oscillation date back to the '60s. In 1957 Pontecorvo discussed $\mu^+e^- \leftrightarrow \mu^-e^+$ [22], and the two-flavour neutrino oscillation physics was worked out by Maki, Nakagawa and Sakata in 1962 [23]. In this model, the oscillation probability was found to be proportional to

$$P(\nu_\alpha \rightarrow \nu_\beta) = \sin^2(2\theta_{\alpha\beta}) \sin^2\left(\frac{\Delta m^2 E_\nu}{4L}\right), \quad (1.7)$$

where the probability of going from the flavour state α to the flavour state β is dependent on its amplitude $\sin^2(2\theta)$, the neutrino energy E_ν , the neutrino flight length, L and the squared difference of the masses of the two neutrino flavours $\Delta m^2 = m_\alpha^2 - m_\beta^2$.

The first experimental evidence of neutrino oscillations came from the Homestake Mine solar neutrino experiment. Between the 1960s and 1980s this experiment, led by physicist R. Davis, used radiochemical technique to measure the flux of solar neutrinos.

Neutrinos from the Sun come from multiple reactions inside the Sun's core. An energy spectrum of the neutrino flux is presented in Figure 1.3. The detector used the

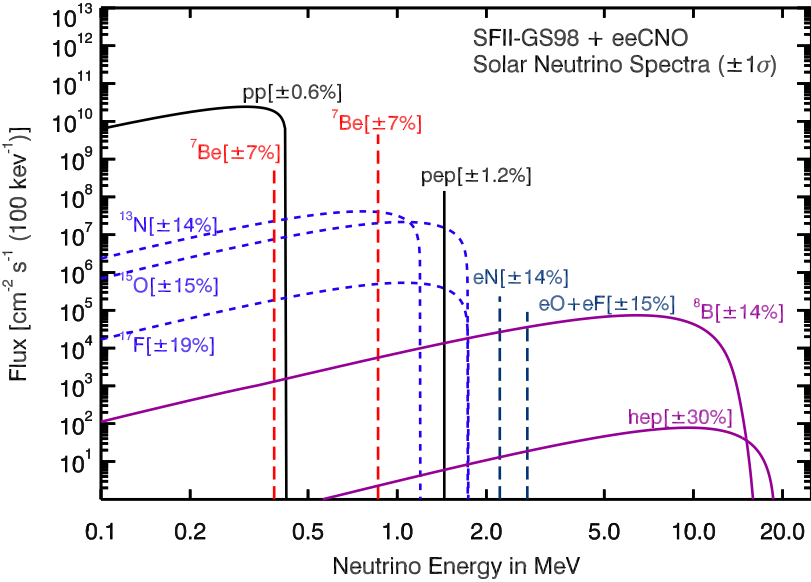


Figure 1.3 Solar neutrino flux produced by all the reactions inside the Sun's core. Taken from [24].

capture process $\nu_e + {}^{37}\text{Cl} \rightarrow {}^{37}\text{Ar} + e^-$, with a threshold of 814 keV, making only ${}^7\text{Be}$ and ${}^8\text{B}$ flux detectable by the experiment. The produced ${}^{37}\text{Ar}$ decayed in ~ 34.8 days and was counted by means of a proportional chamber. Despite the huge number of neutrinos from solar flux $\sim 6 \times 10^{10} \text{ cm}^{-2} \text{ s}^{-1}$, only 1.7 events were expected each day [25, 26]; however, the total flux collected by the Homestake Mine experiment amounted to an observed flux of 0.48 ± 0.04 neutrino interactions per day [27]. This anomalous measurement is referred to the “solar neutrino problem”. To investigate the origin of the “solar neutrino problem” other components of the pp and CNO processes in the Sun’s core, other experiments were developed, with the aim of investigating the lower part of the energy spectrum. In particular, neutrinos from the pp chain are the most abundant, so they were targeted to clarify this problem. In order to measure these neutrinos, the threshold had to be lowered. Using gallium, or gallium-doped targets, the neutrino capture process $\nu_e + {}^{71}\text{Ga} \rightarrow {}^{71}\text{Ge} + e^-$, with a threshold energy of 233 keV it is possible to detect neutrinos from the pp chain. Three experiments followed this idea: the SAGE experiment at Baksan [28], using 50 t of liquid metallic gallium, and the GALLEX [29] experiment at *Laboratori Nazionali del Gran Sasso* (LNGS), using gallium chloride, GaCl_3 . The GALLEX experiment was followed by the GNO experiments, and their data was used for a combined analysis [29, 30]. These results highlighted that also for this lower region of the energy

flux, the model was inconsistent with the data. The same was shown by the results from the SAGE collaboration [28].

The landscape evolved in 1998 with the observation of atmospheric neutrinos by the Kamiokande and Super-Kamiokande detectors. Where the radiochemical detectors measure the reaction rate integrated between extractions, the real-time measurement of solar neutrinos was possible with this experiment. The Kamiokande detector was a 3000 t water-Cherenkov detector in the Kamioka mine. Super-Kamiokande (SK, for short), the successor of Kamiokande, started operation in 1996. It is a large upright cylindrical water Cherenkov detector containing 50 kt of pure water. An inner volume of 32 kt of water was surrounded by 11 000 photomultiplier tubes (PMT), detecting the Cherenkov radiation from the particles inside the volume. Both Kamiokande and Super-Kamiokande can detect solar neutrinos using neutrino-electron elastic scattering (ES), $\nu_\ell e^- \rightarrow \nu_\ell e^-$. The results of Kamiokande and SK for ν_e ES events still showed a decrease of the observed flux (2.308 ± 0.020 (stat.) $^{+0.039}_{-0.040}$ (syst.)) $\times 10^6 \text{ cm}^{-2} \text{ s}^{-1}$ [31], with respect to the expected flux of (5.46 ± 0.66) $\text{cm}^{-2} \text{ s}^{-1}$.

The Kamioka water Cherenkov detector, as well as the Irvine-Michigan-Brookhaven (IMB) water Cherenkov detector, were also able to detect, other than electrons and electron neutrinos coming from the Sun’s core, muons, and muon neutrinos. Those are predicted to be originating in Earth’s atmosphere. Those experiments observed a deficit [32, 33] of neutrinos from what was expected. This constitutes the “atmospheric neutrino problem”. Atmospheric neutrinos come from interactions between cosmic rays and nuclei in the atmosphere, leading to the production of charged mesons, which then decay. One of the leading channels of this chain is the pion decay, $\pi^\pm \rightarrow \mu^\pm + \bar{\nu}_\mu^{(-)}$, and the subsequent muon decay, $\mu^\pm \rightarrow e^\pm + \bar{\nu}_\mu^{(-)} + \bar{\nu}_e^{(-)}$, implying a flavour ratio $(\nu_e + \bar{\nu}_e)/(\nu_\mu + \bar{\nu}_\mu) = 1/2$.

The solution for this “atmospheric neutrino problem” came directly with the SK detector, by following the hypothesis that neutrinos do oscillate, and hence that a deficit of muon neutrinos had to be found as an increase in the population of electron and tau neutrinos. The data collected by SK showed a good agreement for atmospheric neutrinos assuming a two-flavour oscillation [34], with $\sin^2(2\theta) > 0.90$ and $1.9 \times 10^{-3} \text{ eV}^2 < \Delta m^2 < 3 \times 10^{-3} \text{ eV}^2$ at 90 % confidence level. The confirmation for this will come from subsequent experimental efforts, especially from the OPERA detector working at the Laboratori Nazionali del Gran Sasso (LNGS), detecting neutrinos from the CERN Neutrinos to Gran Sasso (CNGS) beam — it did, in fact, detect tau neutrinos [35] from the CNGS ν_μ -disappearance.

The solution for the “solar neutrino problem” came in the early 2000s, with the experimental results by the Sudbury Neutrino Observatory (SNO, for short) [36]. This experiment used 1000 t of heavy water, D₂O, contained in a spherical vessel

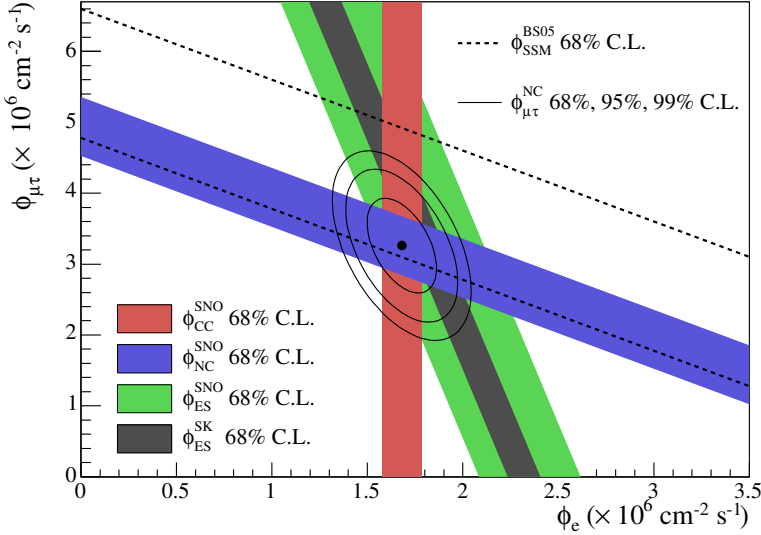


Figure 1.4 Fluxes of ${}^8\text{B}$ solar neutrinos, $\phi(\nu_e)$, and $\phi(\nu_{\mu,\tau})$, deduced from the SNOs CC, ES, and NC results. The standard solar model prediction [25, 26] is also shown. The bands represent the 1σ error. The contours show the 68 %, 95 %, and 99 % joint probability for $\phi(\nu_e)$ and $\phi(\nu_{\mu,\tau})$. The figure is from [41].

surrounded by a H_2O shield. An array of PMTs looked at the Cherenkov radiation produced in both D_2O and H_2O . This way the detector was able to look for multiple signatures of ${}^8\text{B}$ from the Sun's core: in addition to ES scattering in water, heavy water allowed for the detection of CC $\nu_e + d \rightarrow e^- + p + p$, and NC $\nu_\ell + d \rightarrow \nu_\ell + n + p$, where $\ell = e, \mu, \tau$ are all the SM neutrino flavours. Therefore, by comparing the three fluxes (ES, CC and NC), each sensible to one or more neutrino flavours, this detector was able to measure the full neutrino solar flux. The results of the SNO collaboration of CC and NC interactions, combined with the ES events collected by SK, published between 2001 and 2002, allowed the computation of the full flux of neutrinos from the Sun, highlighting that flavour conversion happened also in neutrinos [36–38]. The final test came with the knowledge of neutrino oscillation in matter, through the MSW effect. The mass splitting reported by the SAGE [39] and GALLEX+GNO [40] experiments was in the order of $\Delta m^2 \sim 10^{-5} \text{ eV}^2$, with the oscillation amplitude $\sin^2(2\theta) \sim 0.3$.

Flavour oscillation formalism

In the standard model of particle physics, the flavour oscillation is closely related with the mass mechanism, i.e. how elementary particles get their masses. This is the case for the hadronic sector, where the mass mechanism is linked with flavour oscillation via the V_{CKM} matrix [12].

In the case of neutrinos, there is not *one* mechanism for their masses — there are upper limits to their mass value [42], but since no direct measurement has been made to date, no hypothesis is stronger than others. Any model that aims at providing a valid mechanism for neutrino masses, however, is successful in describing the oscillatory behaviour. The key for describing why neutrinos oscillate lies in what we actually call “neutrinos.” We *cannot* see neutrinos directly as we can, for example, in the case of muons or electrons: we have to look at the products of neutrino interactions to be able to say whether it was an electron neutrino, a muon neutrino, or a tau neutrino. We usually call ν_e, ν_μ, ν_τ neutrinos, but in order to be more formal, we should say that this is the flavour eigenstate basis. As for the quarks, the mass basis can be different from the flavour basis. We define the mass basis as ν_1, ν_2, ν_3 . What I have just said, about neutrinos being only detectable through their interaction products, can be more formally expressed as follows. The flavour eigenstate basis of neutrinos is that which undergoes weak interaction; on the other hand, the mass eigenstate basis is that which undergoes time transformation, and the masses are their eigenvalues, dictating how an eigenstate evolves through time. We can express each base as a rotation of the other, using the complex-valued Pontecorvo-Maki-Nakagawa-Sakata (PMNS) matrix,

$$|\nu_\alpha\rangle = \sum_{i=1}^3 U_{\text{PMNS}, \alpha i}^* |\nu_i\rangle, \quad |\nu_i\rangle = \sum_{\alpha=1}^3 U_{\text{PMNS}, \alpha i} |\nu_\alpha\rangle, \quad (1.8)$$

where the Greek indices indicate the flavour eigenstate basis, and the Roman ones indicate the mass eigenstate basis.

The complex-valued U_{PMNS} matrix can be expressed as the product of three rotations and a complex phase

$$U_{\text{PMNS}} = \begin{pmatrix} 1 & 0 & 0 \\ 0 & \cos \theta_{23} & \sin \theta_{23} \\ 0 & -\sin \theta_{23} & \cos \theta_{23} \end{pmatrix} \times \begin{pmatrix} \cos \theta_{13} & 0 & \sin \theta_{13} e^{-i\delta} \\ 0 & 1 & 0 \\ -\sin \theta_{13} e^{i\delta} & 0 & \cos \theta_{13} \end{pmatrix} \times \begin{pmatrix} \cos \theta_{12} & \sin \theta_{12} & 0 \\ -\sin \theta_{12} & \cos \theta_{12} & 0 \\ 0 & 0 & 1 \end{pmatrix} \quad (1.9)$$

where θ_{ij} are the rotation angles, and δ is the Charge-Parity (CP) violating phase, often referred to as δ_{CP} . The theory, in the case neutrinos were Majorana particles¹, would require two additional phases, α_1 and α_2 . This is obtained by multiplying the PMNS matrix by

$$\text{diag}\left(e^{i\alpha_1/2}, e^{i\alpha_2/2}, 1\right).$$

Given the rotations in (1.8), neutrino oscillation arise from the time evolution of the massive eigenstates ν_i , in vacuum [43]

$$|\nu_i, t\rangle = e^{-ip \cdot x} |\nu_i, t=0\rangle = e^{-iE t + \mathbf{p} \cdot \mathbf{x}} |\nu_i, t=0\rangle. \quad (1.10)$$

Combining (1.8) and (1.10) leads to the flavour basis to oscillate as the mass eigenstates evolve in time (hereafter, $|\nu_i\rangle = |\nu_i, t=0\rangle$ and the same for the Greek indices).

$$|\nu_\alpha, t\rangle = \sum_i U_{\alpha i}^* e^{-iE t + \mathbf{p} \cdot \mathbf{x}} |\nu_i\rangle = \sum_\beta \left(\sum_i U_{\alpha i}^* e^{-iE t + \mathbf{p} \cdot \mathbf{x}} U_{\beta i} \right) |\nu_\beta\rangle. \quad (1.11)$$

The probability of evolving from the initial state β to the final state α at a given time t is given by

$$\begin{aligned} P(\nu_\alpha \rightarrow \nu_\beta) &= \left| \langle \nu_\beta | \nu_\alpha, t \rangle \right|^2 = \left| \sum_i \sum_j U_{\alpha i}^* U_{\beta j} \langle \nu_j | \nu_i, t \rangle \right|^2 = \\ &= \delta_{\alpha\beta} - 4 \sum_{i < j} \text{Re}[U_{\alpha i} U_{\beta i}^* U_{\alpha j}^* U_{\beta j}] \sin^2 \left(1.26 \frac{\Delta m_{ij}^2}{\text{eV}^2} \frac{L/E}{\text{m/MeV}} \right) + \\ &\quad + 2 \sum_{i < j} \text{Im}[U_{\alpha i} U_{\beta i}^* U_{\alpha j}^* U_{\beta j}] \sin \left(2 \times 1.26 \frac{\Delta m_{ij}^2}{\text{eV}^2} \frac{L/E}{\text{m/MeV}} \right). \end{aligned} \quad (1.12)$$

We have made the assumptions that, for $m_i \ll p_i$, since $E = \sqrt{p^2 + m^2}$, $|\mathbf{p}|$ tends to E , and also

$$E = \sqrt{p^2 + m^2} \simeq p + \frac{m^2}{2p} \simeq p + \frac{m^2}{2E}.$$

It is important to highlight — especially for reasons I will present later on (see section 1.3) — that no hypothesis about the number of neutrinos has been made to obtain such oscillation probability. Thus, equation (1.12) is valid for any number N of neutrino families, as long as the mixing PMNS matrix is $N \times N$.

Looking closely at the contributions of (1.12), we highlight three components. The first $\delta_{\alpha\beta}$ is equivalent to not having any oscillation — becomes important in disappearance studies. The second term, proportional to $\text{Re}[U_{\alpha i} U_{\beta i}^* U_{\alpha j}^* U_{\beta j}]$ is closely

¹This is a delicate question; here I am making the hypothesis that three right-handed Majorana neutrinos exist. A model where more than $n = 3$ Majorana neutrinos exists would require more parameters; thus, the PMNS matrix would be different.

related to the mixing angles, but is not sensible in any way to the δ_{CP} CP violating complex phase. This is instead related — thereby measured by looking at — the $\text{Im}[U_{\alpha i} U_{\beta i}^* U_{\alpha j}^* U_{\beta j}]$ term of the equation.

Finally, some remarks are necessary about the equation in (1.12). The first remark is regarding the Majorana phases, introduced briefly after (1.9). As it is clear if we further develop the related math of eq. (1.12), the N -flavour oscillation is not sensitive to the Majorana phases, for which a different type of research is required: this is still strictly related to the problem of neutrino masses and also to the CP violation problem [42, 44], but not dealt with in this thesis.

A second remark is that, as already pointed out when discussing the solution of the “solar neutrino problem” before, the computation presented in (1.12) is valid only for neutrinos propagating through vacuum space. In the case of propagation through matter, it is important to consider the effect such interaction might produce and its impact on neutrino oscillation. This effect was first computed by Mikheyev-Smirnov-Wolfenstein, hence the name MSW effect. This effect shows, starting from the hypothesis that neutrinos in matter interact coherently, how the difference between the electron neutrino flavour — which can interact both through CC and NC coherent scatter with the nuclei —, and the muon/tau neutrino flavours — interacting only through NC coherent scattering — result in a difference of their oscillation probability [45–47]. This effect, while not essential for short baseline experiments such as the SBN program, is core for long baseline experiments, like the Deep Underground Neutrino Experiment [48], and for solar neutrino experiments, which have to take into account the oscillation probability induced by neutrinos crossing the Sun’s radius.

The final remark is about the experimental values of the mass splitting. As I will show later on, with the current status of neutrino oscillation experiments, we have identified two values of mass splitting: one coming from the best fit of atmospheric neutrino oscillations ($\nu_\mu \leftrightarrow \nu_\tau$ oscillations), which I will call $|\Delta m_{\text{Atmospheric}}^2|$, and the other from the best fit of solar neutrino oscillations (mainly $\nu_e \leftrightarrow \nu_\mu$ oscillations), which I will call $\Delta m_{\text{Solar}}^2$. The peculiarity is that these values show two orders of magnitude of difference,

$$\left| \Delta m_{\text{Atmospheric}}^2 \right| \simeq 10^{-3} \text{ eV}^2 \gg \Delta m_{\text{Solar}}^2 \simeq 10^{-5} \text{ eV}^2. \quad (1.13)$$

Since we cannot know, for the atmospheric oscillations, the sign of the mass splitting, there are two possible pictures. The first, called normal ordering or normal hierarchy (NO/NH), assumes a positive sign for both, and so $m_1^2 \leq m_2^2 \leq m_3^2$. The other option assumes a negative sign for the atmospheric mass splitting, and thus $m_3^2 \leq m_1^2 \leq m_2^2$. Figure 1.5 shows an illustration of both NO (left) and IO (right). The mass splitting

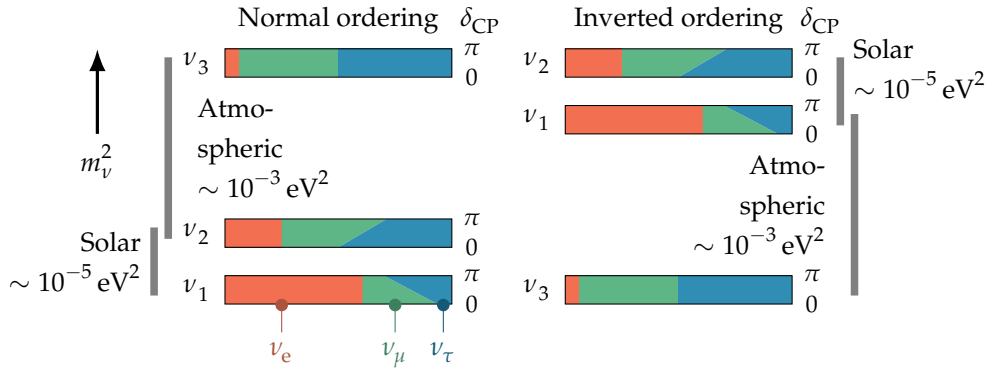


Figure 1.5 The two cases for neutrino mass ordering: the normal ordering, on the left, and the inverted ordering, on the right. The shaded area represents the mixing angles, or the fraction of each flavour in the masses eigenstates. Additionally, the dependence on the CP violating phase effect is shown, with its value ranging from 0 to π . Adapted from [49].

difference also allows, in most cases, to distinctly separate the two oscillation frequencies. This is why, for most short- and long-baseline experiments, it is usually more convenient to approximate the oscillation as a two-flavour oscillation.

Present status

To quantify neutrino oscillations is to measure the parameters of the PMNS matrix. As we can read from (1.9), it depends on three angles and a complex phase, so in order to measure it correctly, multiple experimental measurements must be carried out. Additionally, one aims at knowing the precise value of the mass splittings. Each parameter can be accessed by exploiting different neutrino sources in order to vary the baseline and the energy or the L/E ratio of the measured interaction to pinpoint each parameter in the phase space. Additionally, oscillation measurements are classified either as “appearance” experiments, where the oscillation from one flavour α to another flavour β is measured, or as “disappearance” measurements, where the probability $P(\nu_\alpha \rightarrow \nu_\alpha) = 1 - \sum_{\beta \neq \alpha} P(\nu_\alpha \rightarrow \nu_\beta)$ of getting the same flavour at different distances from the sources is tested.

The distance of the detector from the experimental source is usually selected to maximise the sensitivity to a precise mass splitting, $\Delta m^2 \sim E/L$.

Recently, the precision with which these parameters are determined reached a percent value, allowing neutrino oscillation physics to move from “discovery” field to the “precision” era.

Solar neutrino observations Solar neutrinos have been the first probe for neutrino oscillations and still are an interesting source to both study neutrino oscillations and also to test neutrino interaction in matter. The E/L of neutrinos from the sun, given that $233 \text{ keV} \leq E_\nu \lesssim \text{MeV}$, limits the values of mass splitting to those of the solar mass splitting, $\Delta m_{\text{Solar}}^2 \sim 10^{-5} \text{ eV}^2$. This limits oscillation to mainly a two-flavour oscillation $\nu_e \leftrightarrow \nu_\mu$, so that mainly $\sin \theta_{12}$ is accessible. The complete picture is obtained from multiple years of observations from multiple detectors, leading to a best value of $\Delta m_{21}^2 \simeq 6.92 \times 10^{-5}$ to $8.05 \times 10^{-5} \text{ eV}^2$ and $\sin^2 \theta_{12} \simeq 0.275$ to 0.345 at 3σ . These results come from combining the results from the Soviet-American Gallium Experiment (SAGE) [39], the gallium experiment (GALLEX), combined with the Gallium Neutrino Observatory (GNO) [40], the Kamiokande and SK experiments [50], joined by the BOREXINO experiment [51] and the KamLAND experiment [52].

Atmospheric neutrinos The L/E ratio for neutrinos generated by pion decay in the atmosphere allows exploring the $\nu_\mu \leftrightarrow \nu_\tau$ oscillation phase space that is characterised by a mass splitting $|\Delta m_{32}^2| = |\Delta m_{\text{Atmospheric}}^2| \sim 10^{-3} \text{ eV}^2$, and so allows for the determination of $\sin \theta_{23}$. Atmospheric neutrino oscillations have been studied by the Kamiokande experiment [32] and its successor, Super-Kamiokande [34], by the MACRO experiment [53], and also by neutrino telescopes, such as the ANTARES experiment and the IceCube experiment. Novel experiments will join this research, such as the KM3NeT-ORCA telescope, the successor of the ANTARES experiment, the Hyper-Kamiokande experiment, the JUNO experiment, and the DUNE experiment.

Accelerator neutrinos A similar phase space to that of atmospheric neutrino oscillations can be explored by the accelerator neutrino experiments, especially at long baselines. Accelerator neutrinos can be interesting still, since they provide a large flux with a great purity of the beam. Conventional neutrino beams from accelerators are produced by colliding high-energy particles onto a target — usually p on a ${}^7\text{Be}$ target — producing π and K , which then decay into neutrinos. The branching ratio of $\pi^+ \rightarrow \mu^+ \nu_\mu$ is $\sim 100\%$, with minimal contamination from ν_e and $\bar{\nu}_e$, coming from kaon decays. The values of neutrino energy and baselines are chosen to maximise the oscillation probability, either for studying the atmospheric mass splitting $|\Delta m_{21}^2| \simeq 2.5 \times 10^{-3} \text{ eV}^2$, with the first oscillation maximum at $L/E \simeq 500 \text{ GeV/km}$, or for testing the $\Delta m^2 \sim 1 \text{ eV}^2$ splitting at $\sim 1 \text{ km}$ baselines.

The present landscape of the accelerator neutrino experiments is vast, from the first experiments being the K2K and MINOS experiments — exploring the values of Δm_{31}^2 and Δm_{32}^2 , studying the ν_μ -disappearance channel — to their successor, the

T2K experiment, successor of the K2K experiment, employing Super-Kamiokande as its far detector at 295 km, and the NOvA experiment, collecting neutrinos from the Neutrino at the Main Injector (NuMI) beam at a baseline of 810 km. Both T2K and NOvA measured Δm_{31}^2 , Δm_{32}^2 , and $\sin \theta_{23}$ by measuring both the ν_e -appearance and ν_μ -disappearance channels from a pure ν_μ beam [54–56]. Additionally, both experiments were capable of measuring the δ_{CP} violating phase of the PMNS matrix. The T2K collaboration showed a preference towards $\delta_{\text{CP}} \sim \pi/2$ [55], whereas the NOvA collaboration showed a preference towards $\delta_{\text{CP}} \sim 3\pi/2$ [56].

Reactor antineutrinos Nuclear fission reactors give a substantial flux of electron antineutrinos in the MeV region, through β -decay of radioactive isotopes created during the fission process, primarily ^{235}U , ^{238}U , ^{239}Pu , and ^{241}Pu ; $\bar{\nu}_e$ are then detected at different baselines ~ 1 km. Charged current events cannot happen, given the neutrino energies, for $\bar{\nu}_\tau$ or $\bar{\nu}_\tau$ since they require more energy to produce μ or τ in the final state than what is accessible, so flavour oscillation for such experiments is only accessible through the $\bar{\nu}_e$ -disappearance channel. The detection mechanism is from the inverse beta decay $p + \bar{\nu}_e \rightarrow e^+ + n$, where the signal from the prompt e^+ and the γ (with the energy depending on the type of scintillator; 2.2 MeV for hydrogen, 8 MeV when it is loaded with gallium) from the thermalisation of the neutron helps separate it from the background.

The Kamioka Liquid Scintillator Antineutrino Detector (KamLAND) experiment was one of the first milestones in neutrino physics, detecting neutrinos from multiple nuclear reactors at ~ 180 km from the detector, and detected a ratio of observed inverse β decay over the predicted flux of 0.611 ± 0.085 (stat.) ± 0.041 (syst.) [57], showing evidence for $\bar{\nu}_e$ -disappearance at 99.95 % confidence level.

Reactor antineutrino experiments also showed very high sensitivity to the θ_{13} mixing angle. This is possible by looking at a short baseline ~ 1 km: such searches have been performed by the Double Chooz experiment [58], the Daya Bay experiment [59], and the RENO experiment [60], which found, respectively,

$$\begin{aligned} \sin^2 2\theta_{13} &= 0.086 \pm 0.041 \text{ (stat.)} \pm 0.030 \text{ (syst.)}, \\ &\text{or } 0.017 < \sin^2 2\theta_{13} < 0.16 \text{ at 90 \% CL} \end{aligned} \quad (\text{Double Chooz}) \quad (1.14)$$

$$\sin^2 2\theta_{13} = 0.092 \pm 0.016 \text{ (stat.)} \pm 0.005 \text{ (syst.)} \quad (\text{Daya Bay}) \quad (1.15)$$

$$\sin^2 2\theta_{13} = 0.113 \pm 0.013 \text{ (stat.)} \pm 0.019 \text{ (syst.)} \quad (\text{RENO}) \quad (1.16)$$

1.3 Short baseline anomalies

It is clear at this point that the picture of neutrino flavour oscillation is well established, from the empirical point of view, leading to the clear necessity of a “minimal” extension of the standard model in order to introduce neutrino masses. Since the nature of neutrinos is very different from other particles of the standard model, generating their masses would require a novel mechanism. Multiple beyond SM physics (BSM) models have been developed, many of which would require the addition of particle content to the SM; however strong the evidence for neutrino masses is, no direct measurement has been made to date, and no model is preferred over the others.

In addition to this dilemma, in the past twenty years the picture has been complicated by some anomalous observations that could be hinting at the possibility of a fourth neutrino state. This was suggested by a series of “short-baseline” experiments — for which $L/E \sim 10 \text{ m/MeV}$ [61].

The Liquid Scintillator Neutrino Detector (LSND) at Los Alamos Laboratories detected $\bar{\nu}_e$ from oscillated $\bar{\nu}_\mu$ using a liquid scintillator and observed an excess of electron antineutrinos, with a tension of 3.8σ from the model [62]. This result was tested by the MiniBooNE experiment with different neutrino sources and at a different baseline, which claimed a similar result with a significance of 4.8σ [63]. Reactor antineutrino measurements, which played a significant role in establishing the three-flavour oscillation paradigm for neutrinos, also observed a decrease in flux of electron antineutrinos at baseline distances $< 100 \text{ m}$, with a ratio to the prediction $R = 0.976 \pm 0.024$ [64] — this is the “reactor antineutrino anomaly”. Of equal importance in the discovery of flavour oscillation are the solar neutrino experiments. GALLEX and SAGE [28, 29] employed radiochemical techniques to detect solar neutrinos with gallium; calibration was performed using megacurie radioactive sources and returned anomalous fluxes in the ν_e -disappearance channel, with an observed-expected ratio $R = 0.86 \pm 0.05$, showing a 2.2σ statistical significance: this, corroborated by the results of the BEST experiment — which increased this significance to $\sim 4\sigma$ [65] — constitutes the “Gallium anomaly” (or GA). The combination of these anomalies at short baselines of $\sim 1 \text{ km}$ hints at the existence of a fourth neutrino flavour with a mass splitting $\Delta m^2 \sim 1 \text{ eV}$. This, combined with the fact that only three “active” (i.e. interacting) families of neutrinos are compatible with the experimental results so far [10], lead to the “sterile” neutrino hypothesis: a neutrino that does not undergo weak interaction and is subject to gravitational force.

Pion decay-at-rest accelerator experiments Pion decay-at-rest provide with a very pure muon antineutrino flux with a mean energy of $E_{\bar{\nu}} \simeq 30$ MeV. As such, a detector placed at a relatively short baseline ~ 30 m is sensitive to oscillation with a mass splitting ~ 1 eV². Two major experiments employed this technology to produce neutrino beams, the LSND (Liquid Scintillator Neutrino Detector) and the KARMEN (Karlsruhe Rutherford Medium Energy Neutrino) experiments. Of the two, LSND had the highest sensitivity and observed the “LNSD anomaly”. The KARMEN experiment saw no evidence of such an anomaly, and it is thus considered a “null” experiment for the sterile neutrino framework [66].

The LSND experiment consisted of a cylindrical tank of 8.3 m of height and a diameter of 5.7 m, placed horizontally, filled with 167 metric ton of mineral oil. LNSD detected electron antineutrinos from a beam of muon antineutrinos, produced by pions decaying at rest (DAR). The pions were produced by protons with $E_p \simeq 798$ MeV hitting a target and stopped in water. The signal selection proceeded by looking at both the scintillation light and the Cherenkov light cone produced by the positron (see figure 1.6a for a schematic illustration) correlated with a 2.2 MeV photon signal produced by neutron capture. Scintillation and Cherenkov light were collected by means of 1220 PMTs. The LNSD detector collected data showing an excess of events of 87.9 ± 22.4 (stat.) ± 6.0 (syst.), compatible with the hypothesis of a two-flavour oscillation $\bar{\nu}_\mu \rightarrow \bar{\nu}_e$. The fit pointed toward an oscillation amplitude of $\sin^2 2\theta_{\mu e} \simeq 0.003$ and a mass splitting of $\Delta m^2 \simeq 1.2$ eV², resulting in the allowed regions at 90 % CL and 99 % CL shown in figure 1.6b [62].

Pion decay-in-flight accelerator experiments LNSD’s evidence for this oscillation prompted subsequent searches that needed to be independent. This is why pion decay-in-flight (DIF) was selected as a valid production mechanism: it produces a pure $\bar{\nu}_\mu^{(-)}$ beam with higher energy, providing the opportunity for an independent test at a higher baseline. This was accomplished using the Booster Neutrino Beam (BNB) with the MiniBooNE Cherenkov detector at the Fermi National Accelerator Laboratories (Fermilab) in Illinois, providing a 99.5 % pure muon neutrino beam with a mean energy of ~ 700 MeV. The design of this experiment was made to allow the phase space to align with that of the LNSD experiment: $E/L \sim 30$ MeV/30 m for the LNSD experiment, so the same was accomplished by placing the MiniBooNE detector at 540 m. The MiniBooNE detector consisted of a single tank containing 818 t of mineral oil. The detection was performed looking for Cherenkov radiation inside the tank with 1520 PMTs, and the Cherenkov signature was used to separate between ν_e CC and ν_μ CC events; this selection suffered from backgrounds coming mainly from NC interactions inside the tank and NC π^0 interactions where one ph-

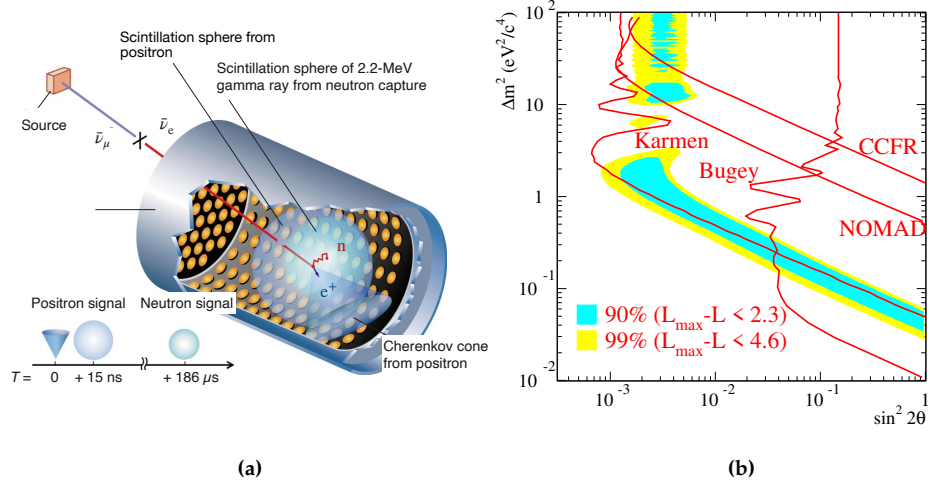


Figure 1.6 (a) Illustration of the LNSD detector at the Los Alamos Laboratories. In the illustration an electron antineutrino interaction is displayed, with both the prompt scintillation light and Cherenkov cone from the positron, as well as the light emitted by the subsequent neutron capture. Adapted from [67]. (b) Allowed regions from the LNSD fit of the sterile neutrino hypothesis in the $(\Delta m^2, \sin^2 2\theta)$ phase space of the oscillation with this state. Taken from [62]

ton from the π^0 decay is not identified. The MiniBooNE experiment took data from 2002 to 2019, collecting a total of 18.75×10^{20} POT (protons-on-target) interactions with both a neutrino mode and an antineutrino mode, showing an excess of events in the signal region $200 \text{ MeV} < E_\nu^{\text{QE}} < 475 \text{ MeV}$, with a statistical significance of 4.8σ [68]. This excess is known by the name of Low Energy Excess, LEE, shown in Figure 1.7.

Reactor antineutrino experiments In the most simple sterile neutrino picture (more about this later in subsection 1.3.1) where one sterile neutrino is assumed, non-zero ν_e disappearance oscillation in neutrinos from reactors should be possible, with detectors placed $< 100 \text{ m}$ from the neutrino source. In such experiments at ILL-Grenoble, Goesgen, Rovno, Krasnoyarsk, Savannah River and Bugey [64], the measured rate of ν_e was found to be in reasonable agreement with that predicted from the reactor antineutrino spectra, though slightly lower than expected, with the measured/expected ratio at $R = 0.976 \pm 0.024$, representing a 2.7σ deviation from the prediction. This is known as the “reactor antineutrino anomaly” (RAA). The addi-

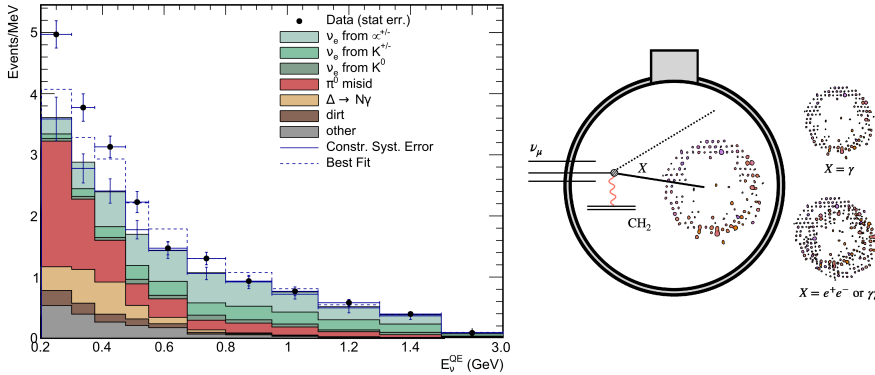


Figure 1.7 (left) Neutrino energy distribution of ν_e CC QE events recorded by the MiniBooNE detector in neutrino mode. The dashed line show the best fit in the sterile neutrino scenario. (right) An example of the type of interactions inside the detector, with different signatures for different final state interactions.

tional measurements by the long-baseline detectors KamLAND and CHOOZ provided a stricter lower result of such ratio, at $R = 0.943 \pm 0.023$, deviating from the unity with a statistical significance of 98.6 % CL.

Radioactive sources experiments Radioactive sources are often used as calibration for different types of detectors. This was the case for both the GALLEX and SAGE solar neutrinos detectors. Such experiments employ natural radioactive sources, either ⁵¹Cr or ³⁷Ar, which both produce electron neutrinos through electron capture processes



placed inside the detector, to calibrate the flux of electron neutrinos with respect to the rate of electron capture processes $\nu_e + {}^{71}\text{Ga} \rightarrow {}^{71}\text{Ge} + e^-$ observed. Both experiments observed a deficit of counts during the detector calibration with respect to the well-known and computed activities of the sources and the cross-section for the measurements, with average ratios \bar{R} ranging from 0.703 ± 0.078 to 0.844 ± 0.031 [69]. A dedicated experiment was planned, the Baksan Experiment on Sterile Transitions (BEST), where a larger deficit was observed, confirming the Gallium anomaly. The combined ratio shows a statistical significance of 4σ , with $\bar{R} = 0.80 \pm 0.04$.

1.3.1 The sterile neutrino hypothesis

The picture presented so far seems to hint, from multiple perspectives, at the possibility of a sterile neutrino scenario. This requires the introduction of a fourth sterile — i.e. not weakly interacting — neutrino state, taking part in short baseline oscillation, with a mass splitting of $\Delta m^2 \sim \mathcal{O}(1\text{eV}^2)$. The need for this state to be “sterile” is required to minimally extend the SM, since the introduction of a massive weakly interacting particle with $m < m_Z/2$ would not be possible.

I claimed before that the PMNS matrix size did not prevent neutrino oscillation from being possible in the current picture. Thus, the most general approach to introducing sterile particle content in the leptonic sector would be to add N sterile neutrinos and consider a $(3 + N) \times (3 + N)$ PMNS matrix. This is correct and the most general way of introducing sterile neutrinos in the model, but to keep the number of parameters in the model as small as possible, it is effectively interesting to look at a “simpler” model, where only one additional sterile family is introduced. This $3 + 1$ paradigm, which is what I will consider moving forward, requires the introduction of a sterile state ν_s , and a basis of four massive neutrinos ν_1, \dots, ν_4 , with the additional assumption that the fraction of ν_s is extremely small for the first three mass eigenstates and near 100 % for the fourth, as illustrated in [Figure 1.8](#).

From the experimental evidence we can assign $\Delta m_{4\ell}^2 \sim \mathcal{O}(1\text{eV}^2)$, and observing that it is greater of both the atmospheric and the solar mass splitting, the oscillation probability can be computed by assuming that both are near zero, giving rise to a two-flavour oscillation probability

$$\begin{aligned} P(\nu_\ell \rightarrow \nu_\ell) &\simeq 1 - 4|U_{\ell 4}|^2(1 - |U_{\ell 4}|^2)\sin^2\left(\frac{\Delta m_{41}^2 L}{4E_\nu}\right) \\ &\equiv 1 - \sin^2(2\theta_{\ell\ell})\sin^2\left(\frac{\Delta m_{41}^2 L}{4E_\nu}\right), \quad \ell = e, \mu \end{aligned} \quad (1.19)$$

$$\begin{aligned} P(\nu_\mu \rightarrow \nu_e) &\simeq 4|U_{\mu 4}|^2|U_{e 4}|^2\sin^2\left(\frac{\Delta m_{41}^2 L}{4E_\nu}\right) \\ &\equiv \sin^2(2\theta_{\mu e})\sin^2\left(\frac{\Delta m_{41}^2 L}{4E_\nu}\right). \end{aligned} \quad (1.20)$$

where the first can be either the disappearance probability of electron or muon neutrinos, and the second controls the appearance probability of electron neutrinos from a beam of pure muon neutrinos. The “effective” mixing angles $\theta_{\alpha\beta}$ are directly correlated with the elements of the extended PMNS matrix in the hypothesis of a $3 + 1$ oscillation scenario.

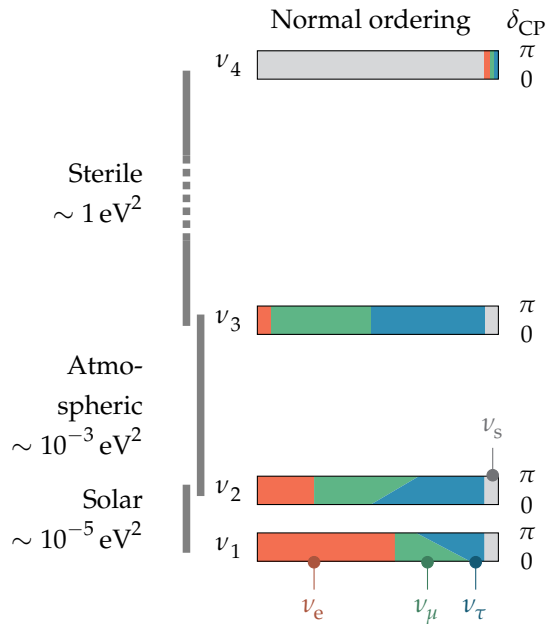


Figure 1.8 Representation of mass ordering, mixing, and splitting in the $3 + 1$ scenario. Normal ordering is assumed for the other three massive states. Expanded from [49].

1.3.2 Experimental status and future perspectives

The current experimental landscape of the sterile neutrino anomalies has broadened, with even more experiments adding limits to the phase space. To this day no definitive picture has completely proved or discarded the existence of this fourth sterile neutrino state.

The experimental landscape can be classified by the channel where it is performing its research and by the result it found (i.e. *did it find any anomaly?*).

One of the strongest experimental anomalies comes from the LNSD experiment. The excess found by this experiment is compatible with the hypothesis of an oscillation picture, suggesting a mass splitting $\Delta m_{41}^2 \simeq 0.2$ to 10 eV^2 . The LNSD experiment was followed by the MiniBooNE experiment. The MiniBooNE LEE in ν_e -appearance analysis is compatible with the results of the LNSD experiment, still preferring a higher mixing angle $\sin^2 2\theta \sim 0.807$ and smaller mass splitting $\Delta m^2 \simeq 0.043 \text{ eV}^2$, compared to that of LNSD. It is interesting to see (for reference, see Figure 1.7) that the $3 + 1$ sterile scenario did not fully explain the excess seen by the MiniBooNE experiment.

Similar to the LSND experiment was the KARMEN experiment, which, however, did not find any signature of $\bar{\nu}_\mu \rightarrow \bar{\nu}_e$ oscillations [66]. The KARMEN experiment operated at similar conditions to those of the LSND experiment, but at a shorter baseline, restricting its allowed parameter space. This posed some limits to the allowed parameter space of the LSND experiment but could not fully cover it all, thus not excluding its claim. Other “null” experiments were performed following the results of LSND and MiniBooNE, including the NOMAD experiment, which operated at a baseline of about 620 m from the source of neutrinos, produced using the SPS accelerator at CERN, with energies of ~ 20 GeV. It excluded at 90 % CL the higher mass splitting values, giving the constraints $\Delta m^2 < 0.4$ eV² (with maximal mixing) and $\sin^2 2\theta < 1.4 \times 10^{-3}$ for large mass splittings [70]. MiniBooNE LEE was explored by many similar experiments; particularly interesting is the MicroBooNE experiment, MiniBooNE’s immediate successor, collecting data from BNB upstream of MiniBooNE at 472 m from the neutrino source. The technology is that of the Liquid Argon Time Projection Chamber [71], which I will describe in great detail later in chapter 2. MicroBooNE found no evidence of the signal excess found by MiniBooNE, looking at multiple final state topologies [72]. These findings were later proved to not be definitive [73] since the rejection of the MiniBooNE claim was not model-independent.

At long baseline multiple experiments also investigated LSND and MiniBooNE LEE anomalies. This is, for example, the case of the ICARUS and OPERA (CNGS1/2) experiments, collecting neutrinos produced from the Sp \bar{p} S in the CNGS beam at an energy of ~ 17 GeV and placed at baselines of 730 km. Both the ICARUS [74, 75] and the OPERA [76] experiments performed analysis excluding much of the parameter space of the MiniBooNE experiment, especially in the high mixing angle region, showing

$$\sin^2 2\theta < 6.8 \times 10^{-3} \quad (1.52 \times 10^{-2}) \text{ at 90 \% (99 \% CL, (ICARUS))} \quad (1.21)$$

$$\sin^2 2\theta < 7.2 \times 10^{-3} \text{ at 90 \% CL. (OPERA)} \quad (1.22)$$

Great tension is also found in very short baselines with reactor experiments. Those look for excess or deficits in the electron antineutrino flux, so it is clear that a correct evaluation of the expected flux of antineutrinos is core for such measurement. For reactor experiments, such a prerequisite is not known with great accuracy and is affected by many systematic uncertainties. Reactor experiments are mostly not sensitive to the spectrum of energies but are considered “rate” experiments, counting the overall excess of the flux, or “spectral” experiments, looking at the energy — or E/L — spectrum. Particularly interesting are the Bugey [77], NEOS [78], PROSPECT [79] and STEREO [80] experiments, which found no evidence of oscillation. NEOS

was followed in its analysis by the RENO, an independent detector sharing the same source, suppressing many of the uncertainties in the flux model, and improving on the results, narrowing even more the parameter space [81].

In the reactor neutrino experiment landscape, an interesting result is that of the Neutrino-4 experiment. This experiment detected electron antineutrinos from a nuclear reactor SM-3 in Dimitrovgrad, Russia, using a detector with the ability to investigate the 6 to 10 m range of baseline distances from the reactor. This experiment gave clear evidence of $L/E \simeq 1$ to 3 m/MeV oscillation, with a sensitivity of roughly 3σ , that is in great agreement with GA experiments such as GALLEX and SAGE — quite unique, since most of the RAA experiments are in tension with GA experiments [82]. When combined with GALLEX, SAGE and BEST its statistical significance rises to 5.8σ [83]. The result of the Neutrino-4 experiment fits well the 3 + 1 scenario, leading to a mass splitting of $\Delta m_{41}^2 = 7.30(0.13)_{\text{stat}} (1.16)_{\text{syst}} \text{ eV}^2 = (7.30 \pm 1.17) \text{ eV}^2$ and an amplitude of $\sin^2 2\theta = 0.36 \pm 0.12$ (stat.).

As I already mentioned, GA experiments differ and are in tension with most of the other experimental searches, requiring a greater mixing angle. This anomaly, found by GALLEX and SAGE and made stronger by the BEST experiment [69], leads to a best-fit point $(\Delta m^2, \sin^2 2\theta) \simeq (1.25 \text{ eV}^2, 0.32)$. The overlap with the allowed regions of the LNSD and MiniBooNE LEE results is negligible, and the overlap with RAA is possible with $\sin^2 2\theta \sim 0.2$.

Another experimental search is in the ν_μ -disappearance and ν_e -appearance channels. These have been the channels explored by NOvA [84], MINOS and MINOS+ [85]. Additional searches in those channels have been performed with data from the IceCube detector, and interesting results will come from the JUNO future neutrino experiment [86].

[Figure 1.10](#) shows a summary of all the experiments that provided exclusion areas in the parameter space, with the baseline at which they are detecting neutrinos and their energy range superimposed to the oscillation maxima in the hypothesis of a two-flavour oscillation scenario.

In this very complicated picture stands the Short-Baseline-Neutrino program [87], to which the next chapter is briefly devoted. In [Figure 1.9](#) are shown the updated allowed and excluded parameter regions from the combination of the multiple oscillation channels and multiple experimental inputs. This experiment will probe the sterile neutrino scenario with increased sensitivity up to 5σ , exploiting a two-detector experimental search in both the ν_e -appearance and ν_μ -disappearance channels.

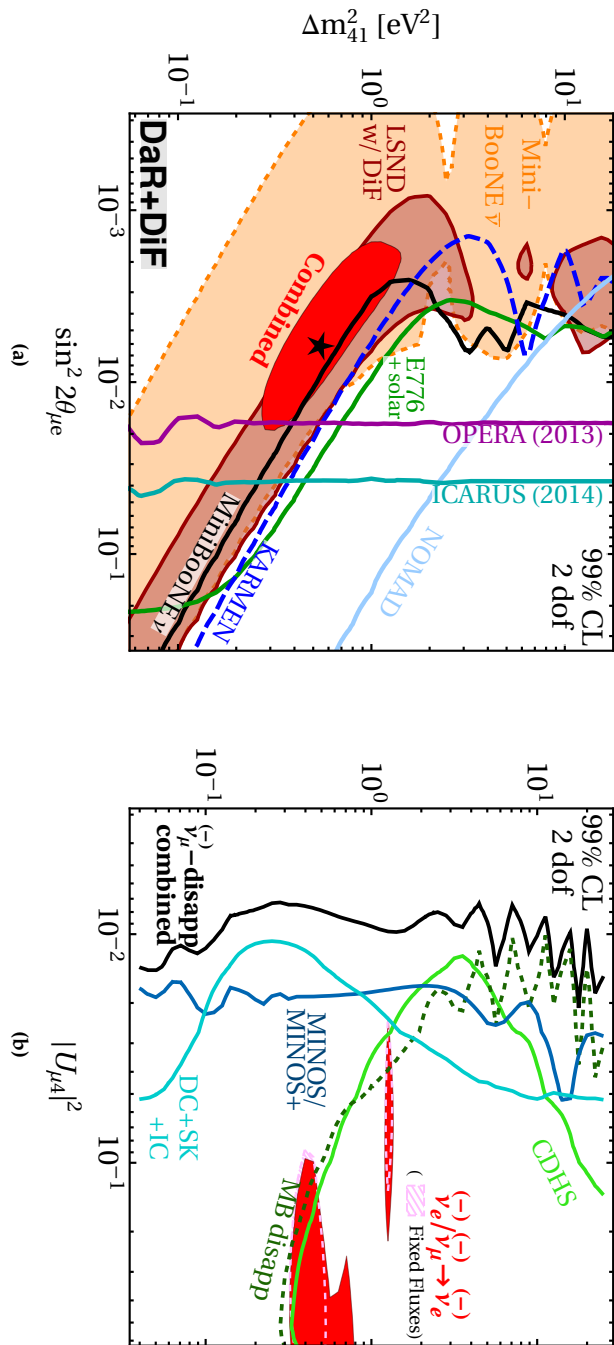


Figure 1.9 (a) Constraints on short-baseline $\nu_\mu \rightarrow \nu_e$ and $\bar{\nu}_\mu \rightarrow \bar{\nu}_e$ oscillations in the presence of sterile neutrinos in 3 + 1 scenarios. (b) Constraints on the 3 + 1 scenario from $\nu_\mu/\bar{\nu}_\mu$ disappearance. Taken from [86].

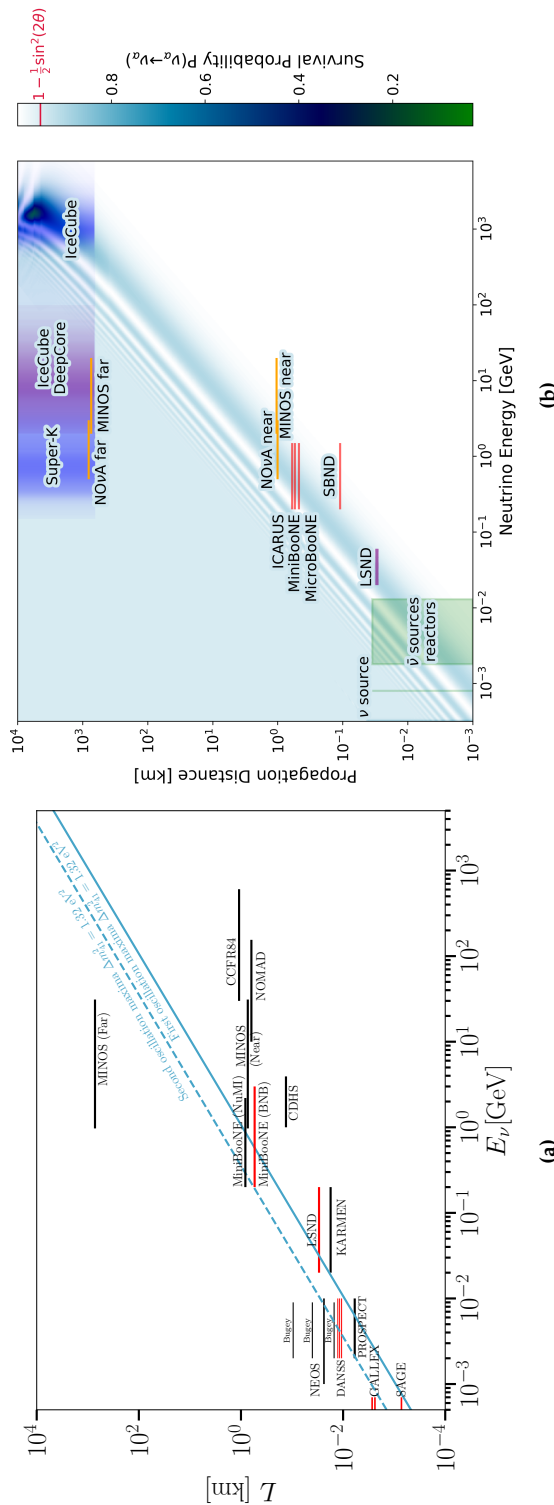


Figure 1.10 (a) Some of the experiments that performed searches for the sterile neutrino states, with their baselines and the energy range they cover. The first and second oscillation maxima are shown in the blue lines. The experiments highlighted in red are those that found a $> 2\sigma$ preference for the additional sterile neutrino state. Taken from [88]. (b) Same plot as for (a), showing other experimental searches. Taken from [89]

2

The SBN program at Fermilab and the ICARUS experiment

2

2.1 The Short Baseline Neutrino program at Fermilab

The Short Baseline Neutrino experimental program at Fermi National Accelerator Laboratories aims to draw a complete and consistent picture of the sterile neutrino scenario, depicted in detail in [chapter 1](#). To achieve a level of statistical significance greater than 5σ for the LSND-allowed region (at 90 % CL), SBN will carry out precision searches, recording millions of NC and CC neutrino interactions on argon.

The key to such high sensitivity, other than the great statistic of events collected, is the design paradigm of the program. It will employ the Liquid Argon Time Projection Chamber (LArTPC) technology [71], with two functionally identical detectors placed at different distances from the neutrino source. This way, the oscillatory behaviour is observed by comparing the neutrino flux at the far detector with the “control” flux recorded at the near detector, reducing the systematic uncertainties related to neutrino production and neutrino interaction in argon.

Albeit the original plan for a three-detector program [87], MicroBooNE finished its data-taking period in 2020, two years prior to ICARUS starting its data collection campaign and five prior to SBND, so the SBN program will perform a search for the sterile neutrino as a two-detector experiment [87, 92].

Both collect data from the common Booster Neutrino Beam (BNB); additionally, the ICARUS detector is located such that it is sensible to off-axis neutrinos coming from the Neutrino at the Main Injector (NuMI) beam.

ICARUS is the far detector for the SBN programme, employing an active mass of 476 t of liquid argon (LAr), at a distance of 600 m from the neutrino source; its position was chosen so as to maximise the oscillation probability. The ICARUS detector started its data taking independently from the SBN program in June of 2022, after the initial commissioning phase. It has now finished the fourth data collection campaign, collecting $\sim 7.54 \times 10^{20}$ POT (proton-on-target), corresponding to about 10^6

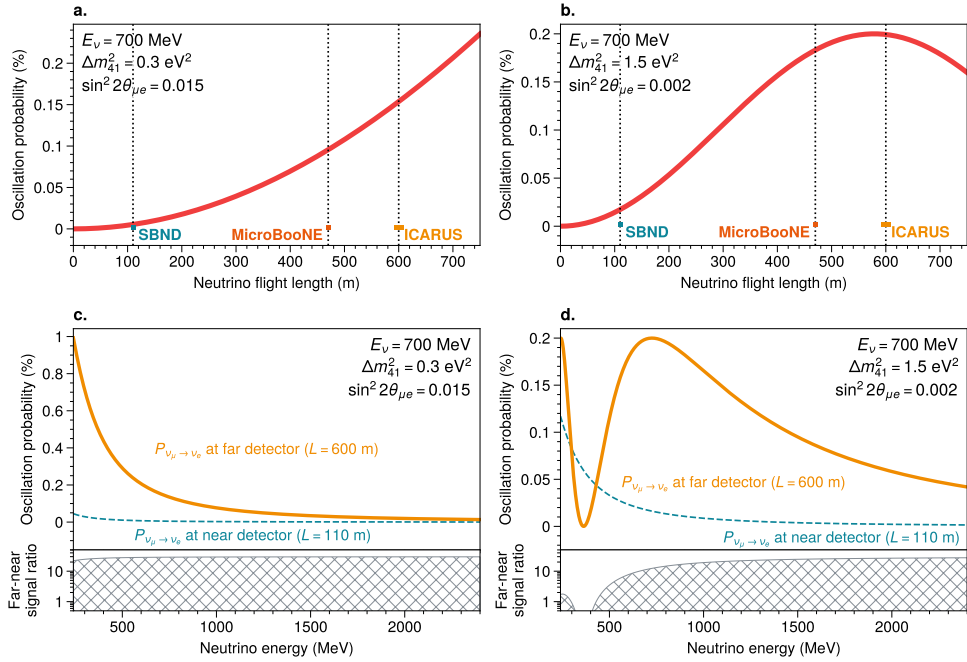


Figure 2.1 (a) and (b) show the oscillation probability for a 700 MeV muon neutrino into an electron neutrino as a function of the length of the neutrino flight using two benchmark values of $(\sin^2 2\theta_{\mu e}, \Delta m^2)$. (c) and (d) show the same oscillation probability as a function of the neutrino energy. Additionally, the bottom panels show the far-over-near ratio. Adapted from [92].

neutrino events.

At a distance of 110 m, SBND is the near detector of the SBN program, with an active LAr mass of 112 t. After commissioning, it started data taking in December of 2024, joining the far detector and allowing for a precise knowledge of the neutrino flux.

Oscillation measurements with a two-detector experiment The main physics goal of the SBN program is the search for a fourth sterile neutrino state in the 3 + 1 model. Using multiple LArTPC detectors, a high-sensitivity search for a high- Δm^2 splitting is possible by studying muon-neutrino oscillations in the $\nu_\mu \rightarrow \nu_\mu$ disappearance and $\nu_\mu \rightarrow \nu_e$ appearance channels.

The oscillation probability for both channels is presented in (1.19) and (1.20) for the disappearance and appearance channels, respectively, with the assumption of the 3 + 1 model. Looking at the $\nu_\mu \rightarrow \nu_e$ appearance channel, from the experimen-

tal results shown in [Figure 1.10](#), the allowed parameter space lies in $\sin^2 2\theta_{\mu e} \in (10^{-3}, 10^{-1})$ and $\Delta m^2 \in (10^{-1}, 10^1)$ eV²; the location of the near and far detector has been optimised to maximise the oscillation probability in this region of parameters. [Figure 2.1](#) show $P(\nu_\mu \rightarrow \nu_e)$ for two benchmark values of $(\sin^2 2\theta_{\mu e}, \Delta m^2)$, assuming a neutrino energy of ~ 700 MeV. Exploiting the strong correlations between the fluxes collected at the near and far detectors — both use the same interaction medium and functionally identical revelation techniques — the major impacting systematic uncertainties, which are those arising from the production mechanisms and the ν -Ar interaction cross-sections, can be mitigated in the two-detector configuration.

With a planned collected statistics of 6.6×10^{20} POT, the $\nu_\mu \rightarrow \nu_\mu$ disappearance channel can also be probed to search for neutrino oscillation mediated by a sterile state. The unitarity of the 3 + 1 PMNS matrix has to be preserved so that in the event of $\nu_\mu \rightarrow \nu_e$ appearance, meaning a nonzero value of $\sin^2 2\theta_{\mu e}$, a nonzero value of $\sin^2 2\theta_{\mu\mu}$, or a $\nu_\mu \rightarrow \nu_\mu$ disappearance signature, should be observed.

Both channels will be studied to either pinpoint the correct $(\sin^2 2\theta, \Delta m^2)$ values or exclude some regions in the parameter space. [Figure 2.2](#) shows the projected excluded and allowed regions of the parameter space in both the (a) ν_e -appearance and (b) ν_μ -disappearance channels of the two-detector operation of the SBN experiment. It should be noted that the projected 6.6×10^{20} POT was the original plan that was presented in the experiment proposal [[87](#)]; however, BNB will operate until 2027, allowing the ICARUS detector to collect three times the statistics in standalone operation.

Additionally, since a nonzero value of both $\sin^2 2\theta_{\mu e}$ and $\sin^2 2\theta_{\mu\mu}$ leads to a nonzero value of $\sin^2 2\theta_{ee}$, both the ICARUS detector, making use of the Booster and NuMI neutrino beams, and the SBND detector, only with data from the Booster beam, will explore the ν_e -disappearance channel $\nu_e \rightarrow \nu_e$. The combined result of this multi-channel search will provide strong evidence in favour of or against the 3 + 1 sterile neutrino scenario.

Cross-sections and BSM physics In addition to the primary physics goals, the SBN programme, with its two LArTPC detectors, delivers a rich physics opportunity.

Starting from particle interaction in liquid argon, both SBND and ICARUS detectors will use the Booster and NuMI (ICARUS-only) neutrino beams to perform cross-section measurements, exploiting the great amount of collected data with both detectors. For SBND, the proximity with respect to the neutrino source leads to a very large flux collected by the detector — each run approximately of 2.2×10^{20} POT corresponds to 1.5M ν_μ and 12 000 ν_e s; the same measurements can be performed

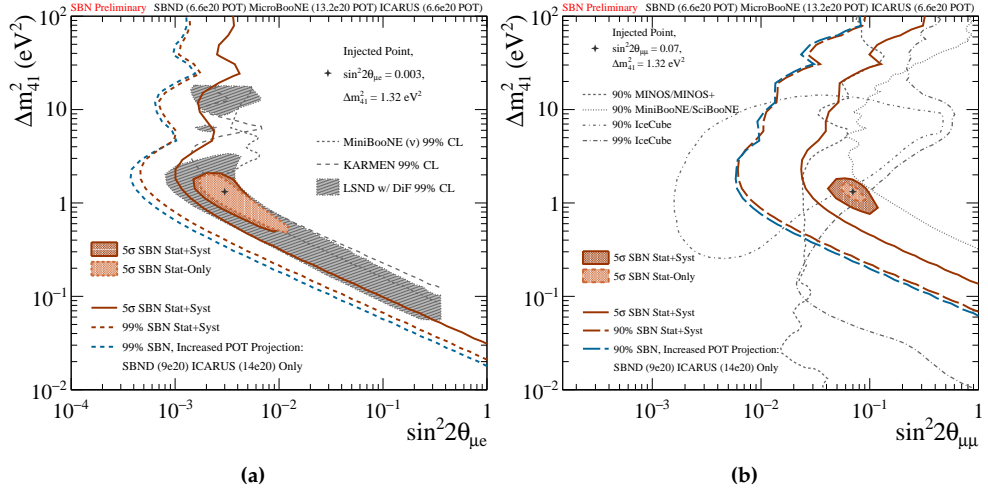


Figure 2.2 (a) and **(b)** show, respectively, the expected sensitivity curves in the ν_e -appearance and ν_μ -disappearance channels under the hypothesis of no observation (solid and dashed lines, respectively at 5 σ and 99% CL) and under the hypothesis of observing an oscillatory signature in both channels (filled regions). These projections account for a collected 6.6×10^{20} POT and a two-detector configuration.

with the ICARUS detector, which at the moment benefits from a longer data collection period and an accumulated statistic of 7.5×10^{20} POT in standalone operation. The larger dimension of the ICARUS detector also allows for more contained events, where all the final state interactions (FSI) are contained inside the detector active volume, allowing for a better particle identification (PID). Additionally, the position of the ICARUS detector allows the collection of neutrinos from the NuMI beam at an off-axis angle of 6° with respect to BNB direction. The added value of the NuMI beam comes from the energy range it covers. Using protons from the Main Injector at an energy of 120 GeV, it is able to cover the 1 to 3 GeV energy range, which overlaps greatly with the DUNE operational energy range. Neutrinos from the NuMI beam will also feature an enriched electronic component from the three-body decay of the kaon, allowing for precise ν_e cross-section measurements. At the moment of writing this thesis, two ν_μ charged current mesonless cross-section analyses, $\nu_\mu CCN > 1p0\pi$ and $\nu_\mu CCNp0\pi$, are being carried on and are in the final phases before publication.

Finally, exploiting the great tracking and calorimetric power of liquid argon TPCs, with exceptional precision and high-performance event reconstruction capabilities, opens up invaluable opportunities for new physics searches. Using high-intensity neutrino beams, with large statistics, it is possible to explore beyond standard model

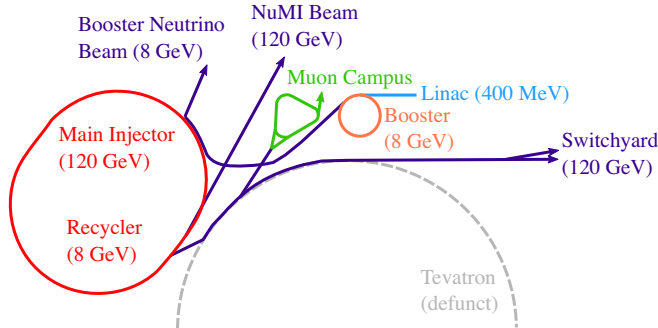


Figure 2.3 Schematics of the accelerator complex at Fermilab. Both Booster and NuMI neutrino beams serve the ICARUS detector, with different energy ranges, 700 MeV for BNB and 2.5 GeV for NuMI. Taken from [94].

theories. A detailed description of possible searches is presented in refs. [87, 92]. Recently the first physics paper by the ICARUS collaboration was published, exploring some of these BSM models involving the scalar sector using data from the NuMI beam [93].

2.1.1 Neutrino beam

The location for the SBN programme was selected to make use of the already existing accelerator infrastructure at Fermilab. Figure 2.3 shows the FNAL accelerator complex schematic overview. This complex provides a powerful beam of neutrinos using protons extracted from the Booster accelerator, core to the operation of the SBN experiment, as well as multiple other particle beams (neutrinos and muons, as well as protons) which are employed in other experiments, such as the Neutrinos at the Main Injector Beam.

The common starting point is the Linac (linear accelerator), boosting protons up to 400 MeV of energy (or ~ 954 MeV of momentum) using radiofrequency (RF) cavities. Accelerated protons are extracted and boosted to an energy of 8 GeV within the Booster ring.

From the Booster ring, a fraction of protons is extracted to be used for the Booster Neutrino Beam, whereas the remaining fraction is sent into the Main Injector accelerator. From there a second Neutrino beam is extracted, the Neutrinos at the Main Injector (NuMI) beam.

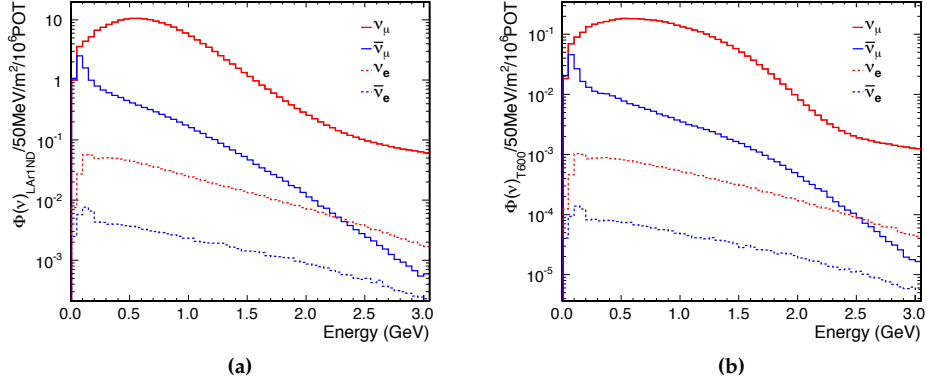


Figure 2.4 Predictions of the neutrino flux as computed by the MicroBooNE collaboration [95] at distances of 110 m (a) and 600 m (b) from the beryllium target, i.e., for the SBND and ICARUS detectors, respectively. Taken from [87].

Booster Neutrino Beam Protons accelerated up to 8 GeV inside the Booster ring are extracted in groups of 81 bunches, each wide ~ 2 ns and 19 ns apart. The repetition rate for the extraction, mainly limited by the focusing horn power supply, is of 5 Hz. Each pulse collides 5×10^{12} p onto a beryllium target. The target is embedded within a pulsed electromagnet (the “horn”) that produces a toroidal magnetic field to focus positive secondary particles and defocus negative secondary particles emerging from proton-beryllium interactions. Charged mesons, which constitute the majority of the secondary particles emerging from p-Be interaction, decay in a 50-meter-long decay region. Within the decay region, charged pions undergo weak decay

$$\pi^\pm \rightarrow \mu^\pm + \nu_\mu^{(-)}, \quad (2.1)$$

resulting in an (anti)neutrino beam. The length of the decay pipe was chosen so as to maximise the muon (anti)neutrino content and minimise the electron (anti)neutrino content coming from the decay of secondary muons

$$\mu^\pm \rightarrow e^\pm + \nu_\mu^{(-)} + \nu_e^{(-)} \quad (2.2)$$

at $\sim 0.5\%$ level. Neutrinos produced by BNB have a most probable value for the energy at $E_\nu \simeq 700$ MeV, and a maximum energy around 2.5 GeV. When the beam is in FHC (forward horn current, selecting primarily positive mesons), the beam composition is dominated by muon neutrinos $\sim 93.6\%$, with neutrinos coming from pion decay and kaon decay for neutrinos with energies greater than 2 GeV; the second major component is given by $\bar{\nu}_\mu$ coming mainly from not-defocused π^- (2.1)

and decaying muons (2.2); the same decay accounts for, together with neutral kaon decays, an intrinsic $\sim 0.5\%$ fraction of $\nu_e + \bar{\nu}_e$.

A detailed study of the beam profile and composition, to allow for precise simulations, was performed by the MiniBooNE collaboration [95], and experimentally verified using the Hadron Production Experiment (HARP). Figure 2.4 shows the beam fractional composition as a function of the energy of the neutrino.

Neutrinos at the Main Injector off-axis beam Once protons are accelerated within the Booster ring, they are then transferred inside the Main Injector ring. There protons are accelerated up to an energy of 120 GeV. The MI circumference is roughly seven times that of the Booster ring, so it can hold up to seven entire Booster cycles in it. However, to make space for the pulse kicker rise time, only six are filled, adding up the spill time to 9.5 μ s: in such time window, NuMI is able to provide a flux of 6.5×10^{13} POT. Protons are collided against a graphite target, and produced mesons decay inside a 675 m long decay tunnel. As for BNB, the main decay products are (2.1) muons and muon neutrinos, with a small fraction of muon antineutrinos and electron neutrinos.

ICARUS is, however, detecting neutrinos from NuMI at an off-axis angle of $\sim 5.7^\circ$ with respect to the detector z coordinate, corresponding to BNB direction. This changes drastically the composition of the beam detected by ICARUS, as off-axis neutrinos and antineutrinos have pretty much the same flux, and overall the fraction of electron (anti)neutrinos is larger. This different beam composition, added to the fact that the energy range is higher than BNB energy range, peaking at 1.5 GeV and extending up to 4 GeV, allows NuMI to be crucial for ICARUS operations: higher energies overlap better with the expected energy spectrum of future experiments, as for example the DUNE experiment, whilst a greater fraction of electron neutrinos allows for the study of both muon- and electron-neutrino argon interaction cross-sections. Additionally, off-axis detection is core for BSM physics searches since it allows to probe the decay of high-energy mesons at high angles with respect to the beam direction. This is the case, for example, for the first physics paper published by the ICARUS collaboration at Fermilab, looking at di-muon final state topologies to probe the existence of long-lived particles (LLPs) in kaon decays involving a di-muon FSI, $K \rightarrow \pi + \text{LLP}(\rightarrow \mu\mu)$ [93].

2.2 Liquid Argon Time Projection Chambers

Core to the high sensitivity of the SBN programme is the shared Liquid Argon Time Projection Chamber technology between the two functionally identical near and far

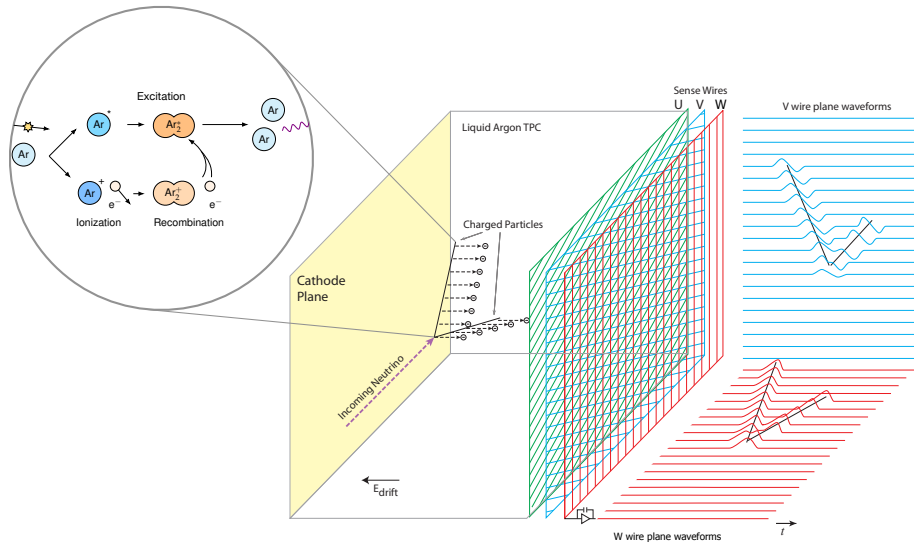


Figure 2.5 Illustration of the working principle of a LArTPC detector. Once neutrinos undergo weak interaction, they ionise the material, producing a large quantity of free electrons that are drifted towards the wire planes. Image adapted from [90].

detectors, respectively the SBND and ICARUS detectors. The Time Projection Chamber technology was first proposed by David R. Nygren [96]. This technology, whose working principle is pictured in Figure 2.5, allows both 3D reconstruction as well as calorimetric capabilities. The basic idea of a TPC detector is that of a large volume, filled with gas or liquid, acting as the interaction medium. Charged particles interact inside this volume, producing ionisation pairs. Free electrons produced in the ionisation process are drifted by means of a strong electric field from the cathode toward the anode, where the ionisation electron charge information is collected by a position-sensitive plane, providing one or more 2D projections of the interaction. The drifting time is used as the third missing component to perform 3D event reconstruction inside the detector.

The first TPCs were built primarily for high energy physics (HEP) applications, and many are still in use for major experiments, such as the ALICE tracker [97]. Carlo Rubbia proposed using liquid argon (LAr) as an interaction target for a TPC, thereby inventing the LArTPC concept for neutrino detection [71]. Liquid argon is an attractive material for particle detection, especially for neutrino physics, given its physical properties

1. LAr has a high density at 1.39 g/cm^3 and a high atomic mass, which, combined

with the small cross-section of ν -Ar interaction, allows for more probable detection than most gases.

2. Being argon a noble gas, it does not attach free electrons, allowing for a longer drift lifetime.
3. It has high electron mobility, $\mu \simeq 320 \text{ cm}^2/(\text{Vs})$ for $E \simeq 0.5 \text{ kV/cm}$ and $T = 87 \text{ K}$, allowing for fast drift velocity $v = \mu E \simeq 1.6 \text{ m/ms}$.
4. The LAr radiation length $X_0 \simeq 14 \text{ cm}$ allows mm-scale calorimetry sampling of neutrino events while having a precise discrimination between electron- and photo-induced electromagnetic showers. Photons produced at the primary vertex usually show a greater conversion gap between the interaction and the starting points of the EM shower; additionally, photo-induced electromagnetic showers display an ionisation pattern in the first centimetres of the shower development compatible with two minimum ionising particles (MIP), whereas electron-induced showers show a pattern compatible with a single MIP.
5. Ar is both easy and cheap to obtain. In Earth's atmosphere, it is the third most abundant gas, and can be liquified using nitrogen: this allows for great scalability required to use it for large-scale detectors.
6. LAr boiling temperature of 87.3 K causes most organic impurities to be frozen out to very low levels. This increases the drift electron lifetime.

Inside a LArTPC, once the neutrino undergoes weak interaction, it produces secondary charged ionising particles. These ionise LAr nuclei, creating Ar^+ , e^- ionisation pairs and producing scintillation light. Roughly 42 ke are produced for each MeV of deposited energy¹, which are then drifted by means of an electric field toward the anode plane assembly (APA). At the anode three planes of wires are placed in sequence, referred to as induction-1 (I-1), induction-2 (I-2) and collection (C) planes — [Figure 2.5](#) shows the common convention, which is to call the three planes U (I-1), V (I-2) and W (C). The planes are properly voltage biased to achieve a nearly perfect transparency of the first two wire planes (I-1 and I-2) with respect to the drift electrons, enabling them to induce a charge on the first two planes and only be collected by the third plane. Given a nominal electric field inside the detector E , a good “transparency” of the successive wire planes to the drifting electrons is obtained by requiring that $E_2 \geq F \times E_1$, and $E_1 \geq F \times E$ — where E_1 and E_2 are respectively the field values in the I-1 to I-2 gap and I-2 to C gap — with the scaling

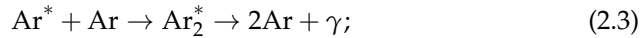
¹This number is dependent on the electric field strength inside the detector. This value is the reference with a nominal electric field of $\sim 500 \text{ V/cm}$.

factor $F \in (1.2, 1.5)$. Due to the ionisation charge inducing a current on the first two planes and depositing the charge only on the third, the signal collected by the three sets of wires is intrinsically different: on the first two, the signal is bipolar, whereas on the third plane, the signal is unipolar.

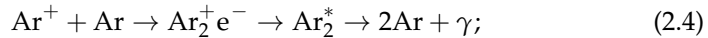
The three planes have their wires orientated at different angles to be able to collect different “projections” of the same interaction happening inside the detector. Using this information, it is possible, in the reconstruction stage, to obtain a $\mathcal{O}(\text{mm}^2)$ -scale (y, z) image of the interaction. The third x coordinate is recovered using the timing information. In fact, when charged particles cross LAr, aside from creating ionisation pairs, they produce scintillation light, which constitutes a prompt signal used to assign the t_0 information. This way, the missing coordinate is reconstructed by comparing the time at which the electron is recorded on the wire with the prompt scintillation reference time t_0 , and knowing the drift velocity of ionisation electrons inside LAr, $x = v_d \times (t - t_0)$.

Contributing to the formation of scintillation light within LAr are two processes, pictured in the inset of [Figure 2.5](#)

- excitation of Ar followed by the formation of the excimer state Ar_2^* , which decay with the production of scintillation photons,



- recombination of ionized argon atoms with a free electron, especially frequent with clouds of e^- around ionized Ar^+ nuclei,



These two processes combined produce 20 000 monochromatic vacuum ultraviolet (VUV) photons per MeV of deposited energy, with a wavelength of $\lambda = 128 \text{ nm}$. This light presents two components, one so-called “fast”, with a characteristic time $\tau \sim 6 \text{ ns}$, and one “slow”, $\tau \sim 1.5 \mu\text{s}$ components. Scintillation light is crucial, as already mentioned, for precise determination of the global timing required to reconstruct the missing coordinate in the 3-dimensional interaction from the 2-dimensional “views”. Additionally, as I will briefly discuss later on, scintillation light is core for double-checking the (y, z) positioning of the interaction, providing the so-called “light barycenter”.

It should be noted, however, that aside from all the mentioned great properties, there are some drawbacks to the use of LAr for particle detection. First and foremost, a complete understanding of the ν -Ar interaction has not been reached yet, so

there are great systematic uncertainties related to the parametrisation of the interaction cross-section. Secondly, in order to keep argon in its liquid phase and minimise the organic impurities, a great effort is required for the design of the cryogenic infrastructure.

Whilst this latter problem is intrinsic to the LArTPC design and requires ad hoc designs and implementations of the cryogenic infrastructure to be optimised, the former problem is addressed in the SBN programme by using two functionally identical LArTPC detectors, which allows the cancellation of many systematic uncertainties when performing a joint oscillation analysis.

Finally, even though LAr was chosen for its large electron mobility, LArTPCs are intrinsically slow detectors, with drift times in the order of milliseconds. Hence, detectors operating at shallow depth, much like the two LArTPCs in the SBN programme, during the readout time window record significant cosmic activity. This reason led both the SBND and ICARUS collaborations to design the detectors to include an external cosmic ray tagger detector system (CRT) with nearly complete 4π coverage to veto most of the cosmic activity.

2.3 The SBN near detector: SBND

The Short Baseline Near Detector (SBND) is the near detector of the SBN programme at Fermilab. Located 110 m from the proton-beryllium interaction target and containing 112 t of liquid argon, the SBND will provide precise flux measurements of unoscillated neutrinos for the far detector, ICARUS. As a “flux monitor”, SBND will greatly reduce the impact of systematic uncertainties related to neutrino interactions in argon and the event reconstruction inside a LArTPC. Following nearly a decade of design, construction, and installation, SBND began operating in July 2024, commencing the collection of stable BNB data at an unprecedented rate of approximately 7000 neutrino events per day in December 2024 [98].

As for the ICARUS experiment, the physics goals of the SBND collaboration extend beyond the search for eV-scale sterile neutrinos; making use of its huge statistics, due to its proximity to the beam source point, SBND will allow for extremely precise ν -Ar interaction cross-section measurements in both the sub-GeV and GeV energy ranges. Additionally, the proximity to the neutrino source point allows the detector to cover both the on-axis as well as the off-axis phase space for BNB, expanding its capabilities to BSM physics studies like what is possible using NuMI for the ICARUS detector.

SBND’s LarTPC consists of a single module, with dimensions of $5 \times 4 \times 4 \text{ m}^3$, holding a total of 112 t of LAr. The structure contains two TPCs sharing two com-

mon cathode plane assemblies (CPAs) at the centre, parallel to the beam direction, and four anode plane assemblies (APAs) at the other two ends. The maximum drift length for the SBND detector is 2 m which, for the nominal electric field of 500 V/cm, leads to a maximum drift time of 1.3 ms. Each APA holds three planes of wires spaced 3 mm apart from each other, each hosting 2816 wires orientated at $\pm 60^\circ$ (I-U and I-2/V, respectively) and 0° with respect to the vertical y axis.

The photon detection system of SBND was developed to enhance the light collection and at the same time provide R&D for future detectors. The first is addressed by making the cathode reflective and also coated in TPB, allowing the full scintillation light to be collected, while shifting the light from VUV to ~ 400 nm, making it detectable by PMTs. The second request for SBND's PDS was addressed by adopting two different light collection systems, PMTs, as for many other LArTPCs, and X-ARAPUCA. These are new innovative light collection technologies developed for the future detectors like protoDUNE and DUNE, adopting the silicon photomultiplier technology for light collection.

The SBND detector finished its commissioning phase last summer and has since started collecting physics data alongside the ICARUS detector for use in the SBN programme.

2.4 The ICARUS-T600 detector

The ICARUS (Imaging Cosmic And Rare Underground Signals) detector, the far detector for the SBN programme, with an active mass of 476 t of liquid argon, is the first ever large-scale operating LArTPC detector. It consists of two identical adjacent T300 modules with internal dimensions $3.6 \times 3.9 \times 19.6$ m³. Each T300 module houses two adjacent LArTPCs separated by a common cathode, with a maximum drift distance of $\simeq 1.5$ m, equivalent to a drift time of ~ 1 ms for the nominal 500 V/cm electric drift field.

The cathode is built up by an array of nine panels made of punched stainless steel, allowing for a 58 % optical transparency between the two drift regions. The anode plane assemblies are made of three parallel wire planes, spaced 3 mm apart; each plane holds 150 μm stainless steel wires orientated on each plane at different angles with respect to the horizontal direction. The wire orientation for the planes in the ICARUS detector is quite unique with respect to other operational LArTPCs. For both TPC in a T300 module, the Induction-1 wires are at 0° . The orientation of the Induction-2 and Collection planes is different for the East and West TPC in each T300 module. [Figure 2.6](#) illustrate this difference. For the East APAs, Induction-2 is orientated at 60° and Collection at -60° , whereas for the West APAs, their orientation

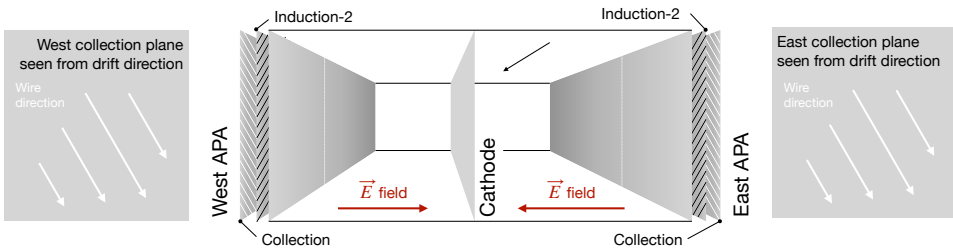


Figure 2.6 Illustration of the wire direction for the I-2 and C planes for the East and West APA for each T300 module. The two side panels show the wire direction as seen by an observer located at the central cathode plane looking in the drift direction.

is reversed, with I-2 at -60° and C at 60° . With this design, as clearly illustrated in the images on both sides of Figure 2.6, electrons drifting from either TPC “see” the wires in both the I-2 and C planes as identically orientated [99].

In total 53 248 wires spaced 3 mm apart with lengths up to 9 m across the three planes are installed inside the detector. By appropriately voltage biasing the first two planes (Induction-1 and Induction-2), a non-destructive charge measurement is provided, whereas the full ionisation charge gets collected by the Collection plane. The three planes are kept at -250 V (I-1), -30 V (I-2) and $+250$ V. The scintillation light is collected by a set of 360 PMTs located behind the wireplanes in the APAs. Photos of the installed planes of wires and PMT mounting are in Figure 2.7.

The two T300 adjacent modules making up the ICARUS detector are housed inside a warm vessel, in which LN_2 is circulated, acting as a cold shield, preventing heat from external thermal insulation from reaching the LAr containers. The external warm vessel uses 60 cm of polyurethane foam to keep argon at its liquid phase just below the boiling point at 87 K. The overall design of the ICARUS detector and the positioning of the two T300 modules are illustrated in Figure 2.8.

The ICARUS collaboration successfully collected neutrino interactions during a three-year run at the deep underground laboratories beneath the Gran Sasso Mountains, LNGS (Laboratori Nazionali del Gran Sasso) from 2010 to 2013 [99]. The nearly 3000 neutrinos collected by the ICARUS detector at LNGS were produced by the CERN to Gran Sasso Neutrinos beam (CNGS) with energy of 10 to 30 GeV using protons from the Sp $\bar{\text{p}}$ S accelerator at CERN.

The ICARUS detector operating at LNGS demonstrated the superior detection capabilities of the liquid argon TPC design: the detector showed a remarkable e/γ separation and particle identification exploiting the measurement of dE/dx versus range. The momentum of escaping muons has been measured by studying the mul-

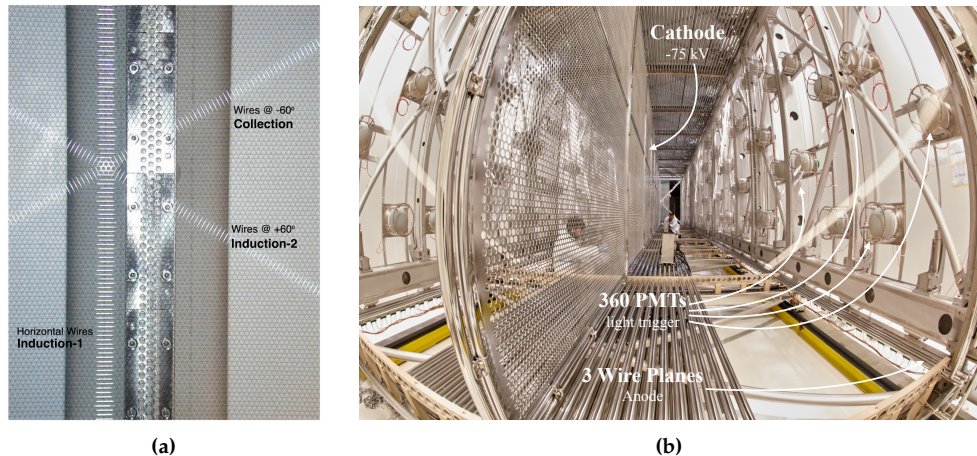


Figure 2.7 (a) shows the three planes of wires as installed in the ICARUS detector. (b) shows one of the ICARUS TPCs’s internals, with the common central cathode on the left and the anode plane assembly on the right, with the PMTs installed. Figures taken from [99, 100].

tiple Coulomb scattering with $\sim 15\%$ average resolution in the 0.4 to 4 GeV energy range.

LNGS operations demonstrated the feasibility of archiving an exceptionally high level of LAr purity, with a < 50 ppt O₂-equivalent level of impurities. In 2013 the low-point record of 20 ppt O₂-equivalent level of impurities was reached [101], corresponding to an exceptionally high electron drift lifetime of 16 ms, marking a milestone for many future experiments, such as the Deep Underground Neutrino Experiment (DUNE). Furthermore, during this activity period, the ICARUS detector probed the sterile neutrino picture alongside the OPERA detector [74–76], providing essential limits toward a better — tough not definitive — understanding of the short-baseline neutrino anomaly.

From 2015 to 2017 the ICARUS detector underwent a thorough overhaul, first at Laboratori Nazionali di Legnano, Padova (Italy) and then at CERN in the Nutrino Platform framework (WA104/NP01 project), where the TPC electronics were updated to withstand the higher throughput a shallow-depth operation could require, as well as the light collection system. It was then moved in 2018 at Fermilab, where it was placed on the BNB baseline at a distance of 600 m from the source target, operating as the far detector for the SBN programme, collecting data from the Booster Neutrino Beam and from the NuMI beam.

All the ICARUS subsystems — TPC, PMT and CRT — were commissioned from

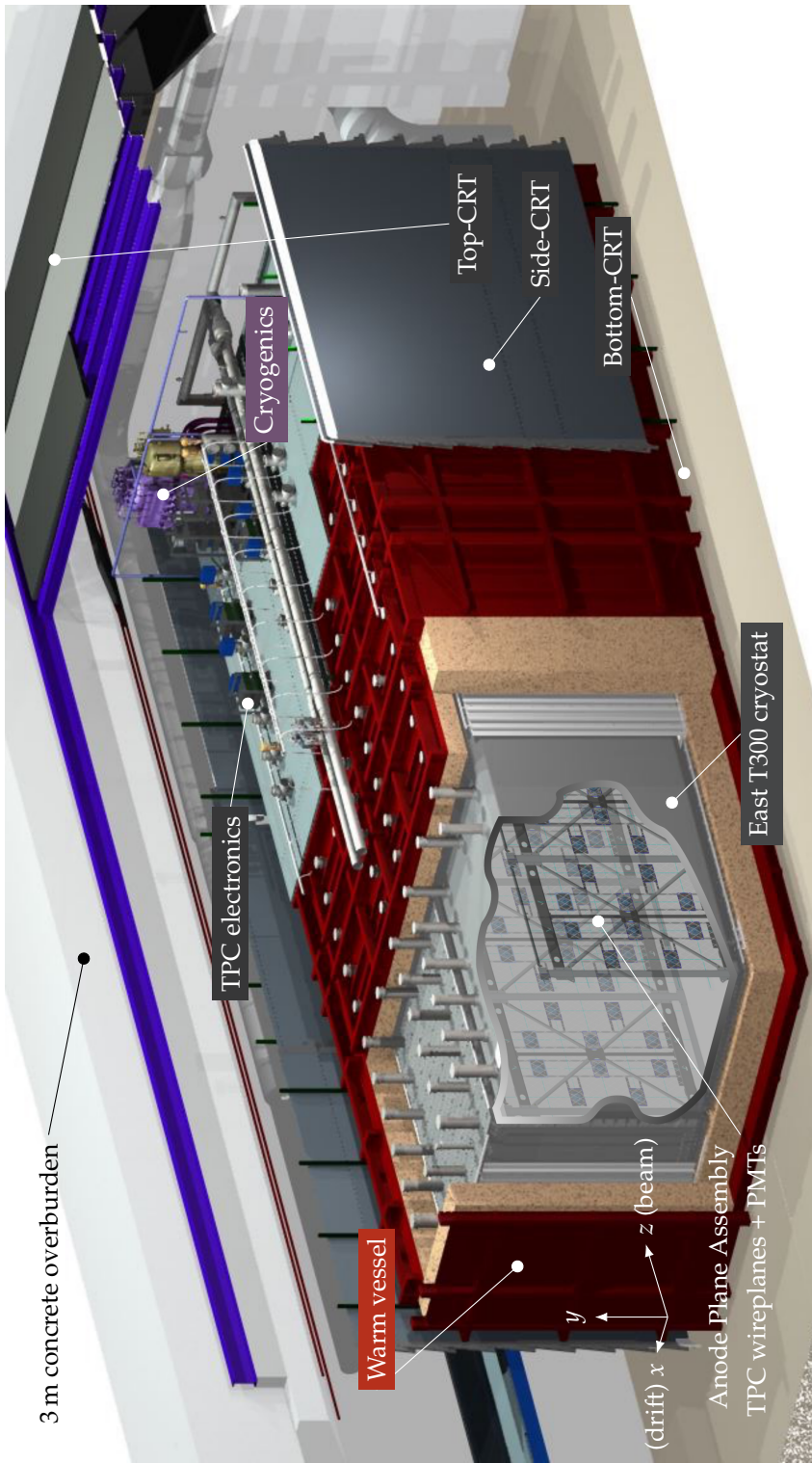


Figure 2.8 Illustration of the ICARUS T600 detector at Fermilab. Surrounding the warm vessel is the 4π coverage CRT. Above the warm vessel, the TPC readout warm electronics are placed, alongside the proximity cryogenics. Inside the warm vessel two identical (east and west) T300 modules, each containing two TPCs sharing a common cathode at the centre and two anode plane assemblies, one on each side.

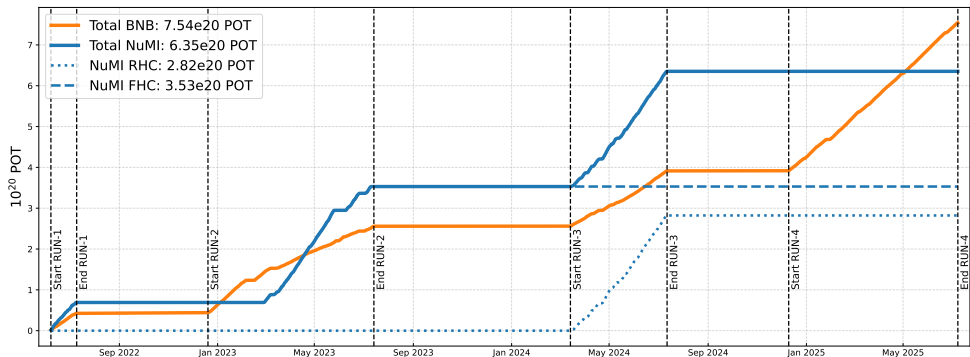


Figure 2.9 Booster Neutrino Beam and NuMI beam collected proton-on-target neutrinos by the ICARUS detector. Courtesy of the run-coordination ICARUS group.

early 2021 to June 2022, when also the deployment of the concrete overburden was completed [100]. This avoids heavy neutral particles entering the TPC volume, resulting in a less noisy event.

After commissioning ended, the first physics data collection run started, lasting until the summer shutdown. Following Run-1, the ICARUS detector was able to collect three more physics runs until the recent summer shutdown. The collected/delivered efficiency is estimated to be greater than 95 %, with a collected 7.54×10^{20} POT for BNB using the FHC mode and a total 6.35×10^{20} POT for the NuMI beam, split between 3.53×10^{20} POT in FHC mode and 2.82×10^{20} POT in RHC mode. Figure 2.9 shows the cumulative POT collected from the start of the ICARUS operations to this day.

2.4.1 The ICARUS subsystems

All three components (sub-detectors or sub-systems) of the ICARUS detector, upgraded during the detector overhauling process at CERN, are essential for the detector operation and to accomplish its physics goal.

TPC One of the largest overhauls performed at CERN was the complete redesign of the TPC electronics [102]. During operation at LNGS, the wires were grouped in bunches of 576 wires, read out and filtered to achieve a unipolar signal from all planes. This was convenient in terms of post-processing but showed strong limitations in the case of intense showers. Such an approach would not have been compatible with the high rates foreseen for the ICARUS shallow-depth operations at FNAL. The new system maintains the previous architecture, which allows for a continuous

triggerable multi-buffered waveform recorder for each wire of the detector with a more advanced design.

TPC wires are grouped together in bundles of 18 cables and feed through the 96 chimneys positioned above the TPC cryostats. At the other end of the chimneys, the signal is read by the front-end electronics, contained in custom-designed mini-crates mounted on the ultra-high vacuum feedthrough mounted on top of the chimneys. The interface between the TPC wires and the front-end electronics is given by the Decoupling and Biasing Boards (DBBs); each DBB is designed to house two isolated 32-channel banks, allowing each TPC wire to be biased at the proper voltage, enabling proper transparency to ionisation charges, and at the same time preventing parallel noise contributions to wire signal from leakage currents. DBBs are designed to operate in GAr (gaseous argon) and can provide a maximum of 400 V of voltage bias. The 53 248 TPC wires are bundled in 1664 32-channel bunches and fed to 856 DBBs on the 96 chimneys: on each chimney flange are installed 9 DBBs, serving 576 TPC wires. It is important to note that, despite both MicroBooNE and SBND having the TPC readout electronic cold to allow for lower noise RMS, ICARUS has opted to keep its TPC electronic partially warm (outside of the TPC cryostat), allowing for easy serviceability.

The analogue signal is then fed to custom-designed CAEN A2795 boards, housing eight amplifier boards, each capable of integrating and digitising eight channels, for a total of 64 channels for each CAEN board. High throughput is accomplished by employing optical fibre connections in a serial link with a bandwidth of 1.25 Gb/s. The digital signal is expressed in units of ADC counts, with the overall TPC electronic giving 1 ADC count per ~ 65 e (or equivalently, $dQ/dx \simeq 1000$ ADC/cm for a MIP, for which $dE/dx \simeq 2.1$ MeV/cm).

Light collection system As mentioned before, once a charged ionising particle crosses liquid argon, ionising it, scintillation light, or VUV photons, is produced from the deexcitation of argon dimers. The light information is crucial for the operation of the ICARUS LArTPC, providing essential information to the event trigger, identifying the interaction occurring in the BNB and NuMI spill gates, as well as calorimetric and position information, useful to complement the 3D track reconstruction by providing absolute timing for each track.

The ICARUS Light Detection System, or LDS, consists of 360 Hamamatsu 8" R5912-MOD PMTs deployed behind the plane of wires (see figure 2.7b). Being the PMT glass opaque to the VUV 128 nm light produced by LAr scintillation, they need to be coated with a $200\text{ }\mu\text{m}/\text{cm}^2$ layer of tetraphenyl butadiene (commonly known as TPB) to convert the VUV light into visible light.

All PMTs are mounted onto the TPC mechanical frames using a supporting system that allows the PMT to be positioned 5 mm behind the Collection plane. A stainless steel grid cage is mounted around each PMT to mitigate the induction of fake signals on the nearby wire planes by the relatively large PMT signals. The PMTs can be calibrated in time with a laser system based on a Hamamatsu PLP10 laser diode, emitting laser pulses with $\lambda = 405\text{ nm}$ and an FWHM of 60 ps, delivered to single PMTs via optical fibres.

Cosmic ray tagger Due to its installation at a very shallow depth at the Fermilab BNB baseline, the ICARUS detector is subject to a high rate of cosmic ray-induced interactions inside the detector volume. These particles are one of the primary background components of multiple neutrino physics analyses, as a muon inside the detector volume could be misidentified as a neutrino interaction. The Cosmic Ray Tagger (CRT) is therefore designed to address this very problem. It fully encloses the detector, covering it from all sides, tagging cosmic muons to clearly identify neutrino interactions.

It is divided into three parts: the top, side and bottom modules. Each of these modules is, in its way, divided to allow for some granularity in the detector, employing the plastic scintillator technology.

The top CRT is designed to cover the top part of the ICARUS detector; placed just below the 3 m concrete overburden, it intercepts almost 80 % of the overall cosmic muon flux. It is comprised of 123 detector modules, each with an area of $1.86\text{ m} \times 1.86\text{ m}$. Each module is made of two orthogonal layers of 8 plastic scintillator bars in which the light is collected by wavelength-shifting optical fibres and read out on both sides by Hamamatsu silicon photomultipliers, enclosed in an aluminium box. The 32 SiPM signals of each Top-CRT module are connected to a CAEN DT5702 Front End Board (FEB) to produce trigger logic based on the coincidence between two SiPMs on the same bar and between two layers in a module.

The side CRT is made using the recovered modules from the MINOS experiment, refurbished with the addition of the SiPM technology to read out the scintillation light.

Finally, the bottom CRT, placed under the detector, is made of 14 modules. Each module, coming from the Double Chooz experiment, is made of polystyrene strips, and the scintillation light is read out by Hamamatsu PMTs.

In both side and bottom CRTs the scintillation light is collected by wavelength-shifter optical fibres that are read out, either on both ends or on one end, by light-sensitive detectors.

3

ICARUS-T600 detector operations and event reconstruction

3

The ICARUS detector, described in section 2.4 is a complex system, and a precise operation is required to make the most out of all its subcomponents. Each part of the online operation is essential and preliminary to the offline operations, consisting of the wireplane signal processing, the reconstruction of all the signals coming from the different subsystems and their combination to obtain a final physics result.

3.1 Data acquisition

The data that comes out of the detector is, much like many other experiments, organised in events. The definition of an event is unique to each experiment, as different experiments collecting different data might prefer one classification type over another. In the case of LArTPC, an event is defined as the collection of the readout signal from all the wires, each with information on the wire position and orientation, and the raw waveform coming from all the other subdetectors modules — CRT and PMT — collected in a time window defined by the properties of each detector starting from a defined t_0 . Being PMTs a fast technology, the time window of the collected waveforms is smaller than, for example, that of the TPC. The start time t_0 is usually defined by means of a triggering system.

ICARUS trigger The ICARUS trigger employs the coincidence between the signal from the beams (BNB and NuMI) spill gates with the scintillation light to provide a global signal that activates the acquisition windows for the TPC and PMT subsystems. For TPC, the acquisition window is driven by the time it takes for drift electrons to cross half of each T300 module: with a nominal electric drift field of 500 V/cm, and a half-width of ~ 1.5 m, the drift time is chosen to be 1.6 ms. The acquisition window for PMTs is driven by the mean lifetime of LAr excited states. De-excitation of LAr produces scintillation light in two components, one fast $\tau \simeq 6$ ns

and one slow $\tau \simeq 1.6\text{ }\mu\text{s}$. To collect the full scintillation light, the time window has to be thus greater than $1.6\text{ }\mu\text{s}$. Additionally, in the case of a second light trigger in the $10\text{ }\mu\text{s}$ immediate subsequent window — this could be the case for a cosmic-induced muon crossing the detector during the drifting of the electrons —, the readout is extended by $7\text{ }\mu\text{s}$. Finally, a $7\text{ }\mu\text{s}$ buffer before the global trigger is also kept, adding up to a total of $26\text{ }\mu\text{s}$ of PMT acquisition window.

The ICARUS trigger architecture allows for multiple configurations, i.e. the acquisition of different types of events [103], with and without beam (on- and off-beam), and requiring or not requiring the PMT light signal (majority or minimum bias). The main ICARUS trigger physics configuration (on-beam majority) is based on the multiplicity of PMT signals in coincidence with the beam “open” spill gate. Off-beam cosmic ray events are collected with similar “off-beam majority”, requiring the coincidence between the light signal and off-beam gates, generated 33 ms after on-beam gates. Minimum bias (both for on- and off-beam configurations) triggers are generated in the presence of the corresponding gate, regardless of the presence of scintillation light.

Collection of the triggered events. Once a global trigger is present, the data acquisition system (DAQ), which communicates via TCP/IP protocol with the trigger system, activates the readout of the whole detector, with 1.6 ms and $26\text{ }\mu\text{s}$ for the TPC and PMTs, respectively. ICARUS DAQ is based on the *artdaq* data acquisition software development kit developed at Fermilab [104]. The *artdaq* SDK provides customisable applications for reading data fragments from detector elements, which are identified as *BoardReader* objects in the *artdaq* language, and configurable applications for performing event-building (i.e. merging together the collected data fragments from each *BoardReader*, performed by objects inherited from *EventBuilder* instances), data-logging and data-dispatch to downstream online data quality monitoring processes.

Customised *BoardReaders* acquire data fragments from all ICARUS subdetectors, TPC, PMT and CRT readout electronics, and from trigger and White Rabbit: this latter subsystem, not described in section 2.4, is a CERN-developed technology that provides global timing across all subdetectors and serves also as a double check against trigger global timing. Event counters and timestamps are assigned accordingly to each data fragment, which are then queued for data transfer to a configurable number of *EventBuilder* instances. When an event is triggered, the corresponding trigger *BoardReader* instance sends the trigger data fragment to the *EventBuilder*. This triggers a request for data from all other configured *BoardReaders* in the DAQ system. Figure 3.1 shows a simplified illustration of the DAQ working

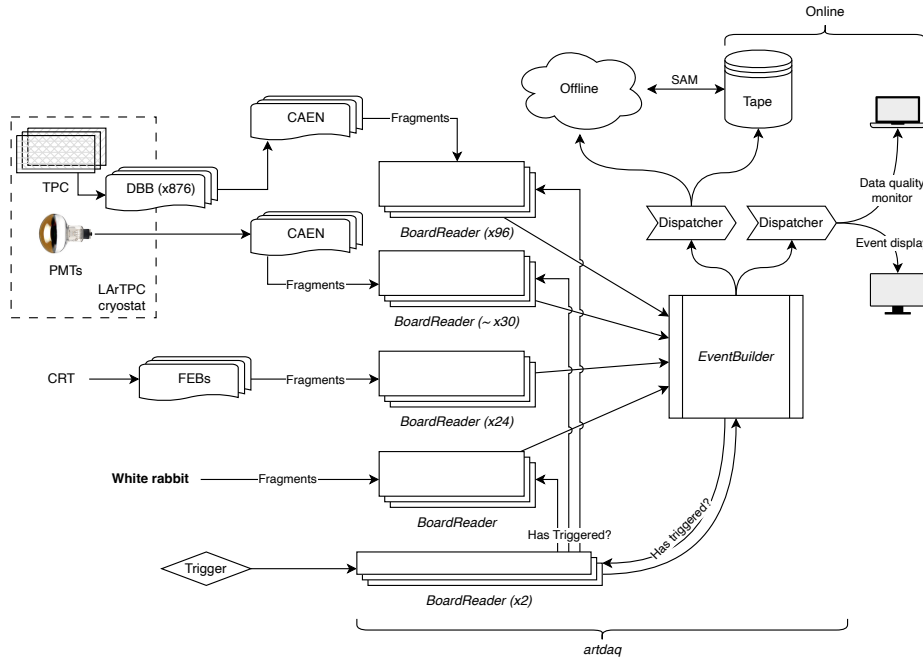


Figure 3.1 Simplified illustration of the ICARUS DAQ system. Further information is found in section 3.1. The number of parallel *EventBuilder* instances could be defined ≥ 1 , to allow for faster processing.

principle.

The data collected by the ICARUS DAQ system is written in different file streams depending on which beam it is detecting and which trigger configuration is active, whether on- or off-beam, minimum bias or majority.

Downstream of the DAQ interface, events are written using the *art* event-processing framework [105] also developed at Fermilab, on which the *artdaq* SDK is built. This allows flawless interoperability between the DAQ interface and the offline analysis, without the need to convert the events saved from the DAQ interface into a format compatible with the high-level offline analysis. After a long testing and commissioning phase, the DAQ system was reported to be able to stably handle high data rates up to 5 Hz. This is, however, well in excess of what the detector is supposed to be handling, given the BNB and NuMI data rates when using a majority-based trigger configuration, based on light scintillation, delivering about 1 Hz of data throughput.

In order to handle the large volumes of data stored on tape, the Fermilab-based SAM (serial access to metadata) system is exploited. This system associates a set

of metadata information with each data file using Python scripts. This metadata is useful in offline analysis to create large datasets of files, identifying whether the files contain raw or processed data, run configuration, run number and so on.

3.2 ICARUS data processing

The output data files contain the aggregated data coming from all the *BoardReader* instances in an event. For the TPC, the data correspond to the digitised waveforms from each TPC readout channel, representing the charge induced by the motion of ionisation electrons drifted by the electric field inside the detector. Similarly, the data from the PMTs correspond to the digitised waveforms of the readout of every PMT inside the detector, corresponding of the scintillation light deposited in each PMT. For the CRT system the DAQ process is slightly different [106–108]. The ICARUS CRTs operate in self-trigger mode [91, 106], whenever a CRT SiPM exceeds the threshold, the data from all 32 SiPM channels for each FEB is stored in internal buffers, holding up to 40 to 80 ms depending on which CRT sub-part is considered. The data from the top, bottom and side CRTs is aggregated within 10 μ s data fragments in the *BoardReaders* instances; once the global trigger is activated, ± 25 ms of CRT data fragments are sent from the *BoardReader* to the *EventBuilder* instance.

The output of all ICARUS sub-detectors is common across LArTPC detectors, which might have different TPC geometry and light collection configurations but share the same underlying technology. The *art*-based *LArSoft* framework [109–111] is the common software development kit providing software infrastructure and algorithms for simulation of Monte Carlo data, processing of both simulated and real data, and event reconstruction. The key to *LArSoft* is the use of real-time configuration files that employ the *Fermilab Hierarchical Configuration Language*, or *FHiCL*, which specify how different modules of the processing chain should be run.

When an event is saved from DAQ to data files and stored to tape, it is then available to be processed. The ICARUS data processing chain is split, like for many other LArTPC detectors, into two *stages*, usually named *Stage0* or *reco1* and *Stage1* or *reco2*. Processing the raw collected data is a mandatory step in order for it to be properly analysed.

In the *Stage0/reco1* step, all data from the three sub-detectors is processed to produce a “simpler” description of the raw signal. This means to decode the raw signal and translate it into objects in the *LArSoft* format for offline reconstruction. It also performs signal processing of the waveforms to identify physical signals, *Hits*, that can then be used as input to the higher-level event reconstruction tools implemented in the *Stage1/reco2* steps.

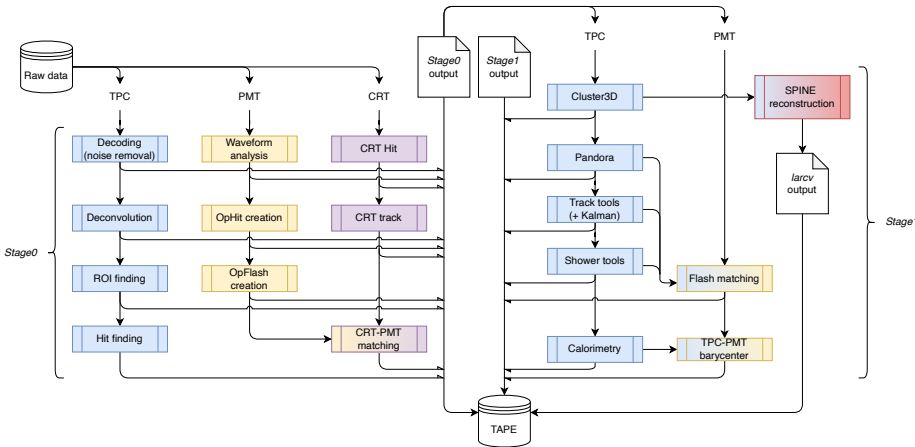


Figure 3.2 Illustration of the data processing pipeline used in the ICARUS detector showing the steps involved in both *Stage0* and *Stage1*.

3

Figure 3.2 pictures the overall *Stage0/Stage1* chain which is applied to the data files produced by the ICARUS DAQ. A detailed description of these steps follows in the next paragraphs.

3.3 Light reconstruction

One of the first steps in *Stage0* reconstruction addresses the reconstruction of the light signal. Reconstruction of the light signal associated with the event of interest is based on the recorded PMT signals in the events, sampled at 500 MHz. For any event triggered in coincidence with the beam spill, the digitised signals of all 360 PMTs are recorded in 30 μ s long time intervals. In addition to this data, whenever an off-time cosmic ray event crosses the volume, triggering scintillation light acquired by the PMTs in the ± 1 ms around the beam gate, all 180 PMTs belonging to the T300 module containing the interaction are recorded in 10 μ s long time intervals.

The first step in the light reconstruction is the identification of the PMT signal, using a threshold-based approach. To do so, a “baseline” has to be defined, which is performed by a sliding window. The pedestal (the *baseline*) is used to then identify the signal over the threshold, using three thresholds defining the start, tail and end points of the PMT hit, called *OpHit*. The algorithm identifies an *OpHit* as the ensemble of these three values and some information about the integral collected charge of the PMT, which is proportional to the light collected. If a start threshold is reached before the end of a previous *OpHit* the hit is truncated. Figure 3.3a shows

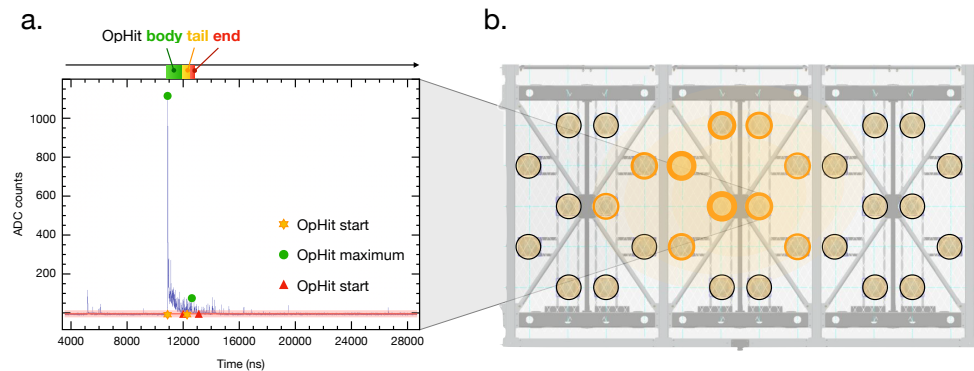


Figure 3.3 Illustration of an interaction as seen by the PMTs inside the detector volume. (a) shows the pedestal-subtracted waveform produced by a single fired PMT, with the *OpHit* information is clearly marked on top, with the three regions (body, tail and end) highlighted. (b) shows all the PMTs activated during an event in the TPC volume; the PMTs which are over threshold, coloured yellow, will constitute the *OpFlash* object.

the example of a PMT with a clear single *OpHit*.

After individual optical hits are reconstructed, they are clustered together into higher-level objects, called *OpFlash*, corresponding to multiple optical hits happening in proximity inside the detector, hence corresponding to the same physical event inside the volume. Figure 3.3b shows multiple PMTs whose *OpHit* are going to be clustered into a single *OpFlash*, corresponding to collected light produced by a single interaction inside the detector.

All data products created in the *Stage0* PMT processing are saved using the same *LArSoft*-based structure to ROOT [112] files.

3.4 Wireplanes signal reconstruction

After the PMT data has been processed, it is time for the TPC wire data. The wire data is the waveform readout of the 53 248 individual wires, with coherent noise removed by the readout cards. Only minimal further processing is performed online, which leaves more scope for reprocessing the raw data using improved signal processing tools. The recorded waveforms are in ADC count/tick units, where the amplitude of the signal is expressed in ADC counts and the time information in ticks, each corresponding to 0.4 μ s in the ICARUS TPC timing. Figure 3.4 shows a sample of the data collected by the three planes, exhibiting the characteristic bipolar shape

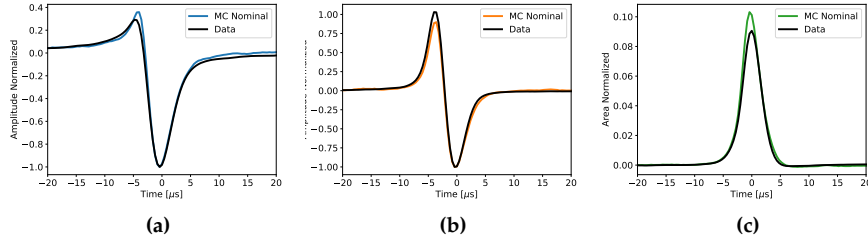


Figure 3.4 Typical *raw* signal captured by the three planes (induction-1 (a), induction-2 (b) and collection (c)) showing the characteristic bipolar signal for the two induction plane and the unipolar shape for the collection plane. Taken from [113].

3

for the two induction wire planes and a unipolar signal for the collection plane.

In order to obtain a simplified representation of the information collected by the wireplanes, three major steps are addressed in *Stage0*: 1. the wire signals are deconvolved from the TPC electronic response functions, so that all three wire signal are also unipolar in shape; 2. the signal is analysed in order to define the region-of-interest (ROI) with a threshold-based algorithm; 3. each ROI is finally fit using a Gaussian function, whose area is proportional to the number of drift electrons generating the signal.

Wire signal processing The raw decoded wire signal shape is dependent on the distribution of drift electrons, which is core to obtaining calorimetric and particle identification information, but in order to explain such dependency, the raw signal must be processed. The resulting signal $R(t)$ on the wires can be seen as the convolution of serial effects of signal formation, electron propagation, electrostatic field response around the wires and processing by the DAQ to the true electronic signal, so that the response function can be factorised as

$$R(t, t') = \text{Ionization} \otimes \text{Recombination} \otimes \text{Diffusion and Attachment} \otimes \text{Field response} \otimes \text{Electronic response} \otimes \text{Electronic noise} \quad (3.1)$$

In order to recover the desired ionisation electron yield, useful to have a knowledge of the deposited energy per wire inside the detector as a function of time, it is necessary to unfold these effects.

The ICARUS detector exploit a signal processing chain similar to other LArTPC experiments, performing a deconvolution in time of the signal waveforms. Ideally, after the deconvolution step, the signal pulse produced by a charged track on the wire would be Gaussian-shaped, with an integral area proportional to the deposited

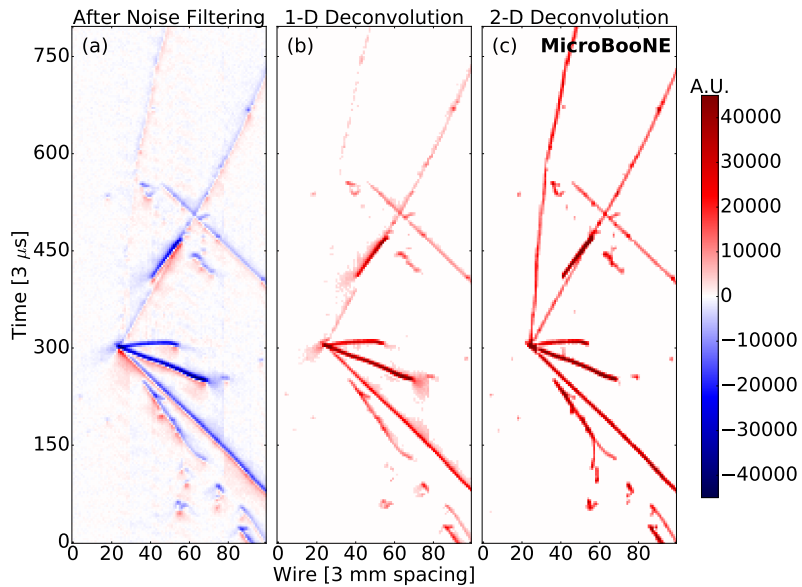


Figure 3.5 Example of the effect of signal processing using the one-dimensional deconvolution approach used in ICARUS (b) with respect to the noise-filtered data (a). (c) shows the same event using a two-dimensional deconvolution approach, performing the deconvolution both in the time direction as well as in the direction of the wires. Taken from [114].

energy inside LAr. The signal recorded on the wires is the convolution of the response function R with the “true” S signal,

$$M(t') = \int_{-\infty}^{+\infty} R(t' - t) S(t) dt; \quad (3.2)$$

Using the properties of the Fourier transforms, this can be written in the frequency space as $\mathcal{M}(\omega) = \mathcal{R}(\omega) \cdot \mathcal{S}(\omega)$, which can be easily inverted, retrieving the “true” signal shape $\mathcal{S}(\omega)$. This approach, referred to as “one-dimensional” deconvolution, is currently employed in most of LArTPC detectors. However, this assumes that the charge distribution on each wire is independent on the charge distribution on the wires in its vicinity. It has been demonstrated that this is not completely true, as can be seen in references [114, 115]. Though it implies small corrections to the overall deposited charge in general, this is not always the case. For example, for isochronous tracks (i.e. tracks lying parallel to the wires, which is somewhat common for the induction-1 wires given the ICARUS geometry), these vicinity effects can create destructive interference patterns.

In [114, 115] a solution, adopting two-dimensional deconvolution techniques over

both the wire time as well as the wire number, is presented; this provides a strong and computationally efficient method to better extract the distribution of ionisation electrons. Figure 3.5 shows the result of the 1D and 2D approaches as tested by the MicroBooNE detector. Tests towards adapting the 2D signal deconvolution are being made inside the ICARUS collaboration, and once validated, should provide a better reconstruction efficiency for the ICARUS TPC detector.

ROI finding Once the signal is unipolar in all planes, the next step to define the TPC hits is to select only the “interesting” regions of the wires. These regions of interest (ROI) are identified by performing a threshold search in the time domain, allowing to restrict the area on which the *Hits* are created to small portions of the wires. ROIs can be actually relevant to iteratively improve the performances of the 1D/2D deconvolution steps, minimising the time-domain region over which the deconvolution is performed. Once ROIs are identified, a baseline value can be assumed for all other times in the waveform, drastically reducing the size of these data products inside the data files.

Hit creation Upon the identification of ROIs, the final step is the creation of the *Hits* objects. A *Hit* is a two-dimensional object representing a cluster of electric drift charges, arriving at a certain time on a certain wire. The *Hit* finding algorithm runs under the assumption the distribution of the drift charges is gaussian. Operating on the deconvolved ROI segments of the waveforms, it tries to fit one or multiple Gaussian distributions onto the signal shape. The extracted parameters from the fit process of the Gaussian distribution(s) — the area, FWHM, the mean, and their multiplicity — are the properties of the *Hit* objects. The area is proportional to the cumulative charge deposited by the electrons, proportional to the deposited energy inside the detector; the mean and the FWHM represent the *Hit* peak time and its width; the multiplicity can be used to perform operations between adjacent hits.

At this point, a collection of 2D *Hits* for each plane of wires has been created. The three 2D views of the planes are stored and used as input for the event reconstruction taking place inside *Stage1*.

3.5 Cosmic ray tagger reconstruction

The first step in the reconstruction of the CRT signal is the extraction of the number of photoelectrons $n_{\text{p.e.}}$ extracted from the ADC count, knowing the amplification

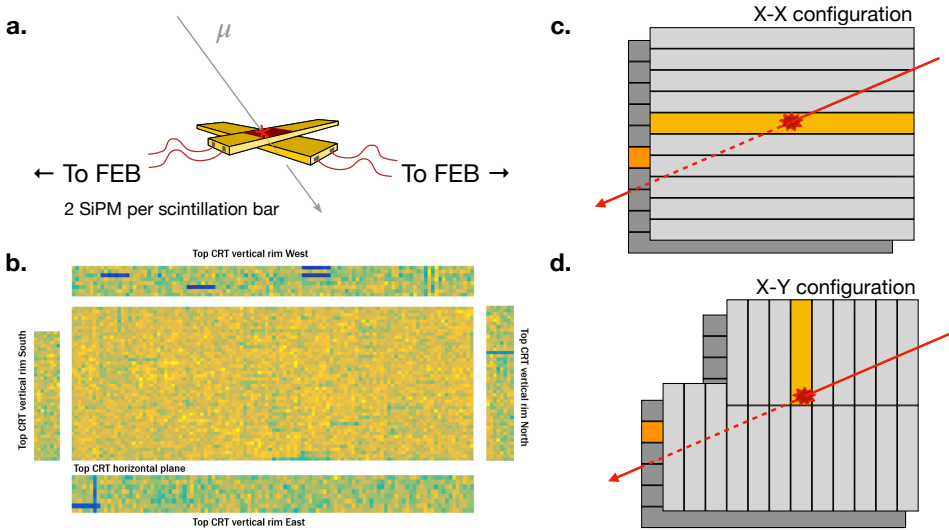


Figure 3.6 Illustration of CRT *Hit* reconstruction position. (a) shows the reconstruction for the top CRT modules, where the coincidence between two scintillation bars is required. (b) shows the distribution of the CRT hits reconstructed in the different regions of the Top CRT. Blue regions correspond to malfunctioning channels. (b) is taken from [107], (a), (c) and (d) are adapted from [91].

gain, subtracting the pedestal

$$n_{\text{p.e.}} = \frac{\#\text{ADC} - \text{ped}}{G}. \quad (3.3)$$

A preliminary selection for the side CRT data is performed, requiring a 7.5 pe threshold. The top CRT does not require a preliminary selection based on a threshold but instead requires a quadruple coincidence to generate a *Hit* (see Figure 3.6a). At this point it is possible to create the CRT *Hit* objects for side and top CRTs. To each *Hit* object are associated two timestamps, T_0 identifying the global timing of the recorded *Hit*, provided by the White Rabbit switch system and T_1 which identifies the relative timing of the *Hit* with respect to the trigger. Additionally, the CRT *Hits* contain the position in the ICARUS detector frame of reference. Due to the differences in the CRT modules between side and top CRT, the position computation is slightly different.

By exploiting the quadruple coincidence, the top CRT *Hits* local position in each module with a known granularity of $23 \times 23 \text{ cm}^2$. A transformation is all that is required to know the *Hit* position with respect to the ICARUS detector frame of reference. Figure 3.6b shows the distribution of the CRT *Hits* using a collected calibration

run.

For the side CRT modules the reconstruction is slightly different. The coincidence of adjacent layers is reconstructed offline at the software level, due to same modules being read by multiple FEBs. *Hit* scintillator strips are identified by selecting in each FEB the channel that generated the FEB trigger signal, which is the one with the highest charge amplitude. [Figure 3.6c](#) and d show two of the configurations of the CRT side module strips. The triggering strip is shown in yellow, and the red star shows the interaction point. The north, east and west side CRTs have the X-X configuration pictured in [Figure 3.6c](#). For these, if two opposite SiPM signals are collected within 150 ns, and read out by two FEBs, the longitudinal position (across the strip) can be computed with respect to the centre position of the strip by comparing the T_0 timestamps recorded by each FEB,

$$z = (T_B - T_A)/2 \cdot v_{wls}, \quad (3.4)$$

where T_A and T_B are, respectively, the two timestamps recorded by the FEBs, z is the computed longitudinal position, and v_{wls} is the group velocity of the light signal inside the wavelength shifter fibre. The south CRT wall is using the X-Y configuration shown in [Figure 3.6d](#), for which a software coincidence similar to that of the top wall is performed, exploiting the orthogonal relative position of the outer and the inner strips.

The last step performed in *Stage0* concerns the temporal matching of the light and CRT information. This step is crucial, especially for higher-level processing, where it can be exploited to improve the efficiency by which correct interactions are selected inside the detector, rejecting out-of-time activity using the CRT-PMT match.

Bibliography

1. J. Chadwick, "The intensity distribution in the magnetic spectrum of β particles from radium (B + C)", *Verh. Phys. Gesell.* **16** (1914) 383–391. [Cited on p. 5](#)
2. W. Pauli, "Dear radioactive ladies and gentlemen", *Phys. Today* **31N9** (1978) 27. [Cited on p. 5](#)
3. E. Fermi, "Tentativo di una Teoria Dei Raggi β ", *Il Nuovo Cimento (1924-1942)* **11** (Jan, 1934) 1–19. [Cited on p. 5](#)
4. E. Fermi, "Versuch einer Theorie der β -Strahlen. I", *Zeitschrift für Physik* **88** (Mar, 1934) 161–177. [Cited on p. 5](#)
5. C. L. Cowan, F. Reines, F. B. Harrison, H. W. Kruse, and A. D. McGuire, "Detection of the free neutrino: A Confirmation", *Science* **124** (1956) 103–104. [Cited on p. 6](#)
6. C. D. Anderson and S. H. Neddermeyer, "Cloud chamber observations of cosmic rays at 4300 meters elevation and near sea-level", *Phys. Rev.* **50** (Aug, 1936) 263–271. [Cited on p. 6](#)
7. S. H. Neddermeyer and C. D. Anderson, "Note on the nature of cosmic-ray particles", *Phys. Rev.* **51** (May, 1937) 884–886. [\(Not cited.\)](#)
8. J. C. Street and E. C. Stevenson, "New Evidence for the Existence of a Particle of Mass Intermediate Between the Proton and Electron", *Phys. Rev.* **52** (Nov, 1937) 1003–1004. [Cited on p. 6](#)
9. B. Pontecorvo, *Electron and muon neutrinos*. Cambridge University Press., 1991. [Cited on p. 6](#)
10. ALEPH Collaboration, D. Decamp *et al.*, "A Precise Determination of the Number of Families With Light Neutrinos and of the Z Boson Partial Widths", *Phys. Lett. B* **235** (1990) 399–411. [Cited on pp. 7 and 22](#)

64 *Bibliography*

11. M. L. Perl, *et al.*, “Evidence for anomalous lepton production in $e^+ - e^-$ annihilation”, *Phys. Rev. Lett.* **35** (Dec, 1975) 1489–1492. [Cited on p. 7](#)
12. M. E. Peskin and D. V. Schroeder, *An Introduction to quantum field theory*. Addison-Wesley, Reading, USA, 1995. [Cited on pp. 7 and 16](#)
13. M. Goldhaber, L. Grodzins, and A. W. Sunyar, “Helicity of neutrinos”, *Phys. Rev.* **109** (Feb, 1958) 1015–1017. [Cited on p. 7](#)
14. UA1 Collaboration, G. Arnison *et al.*, “Experimental Observation of Lepton Pairs of Invariant Mass Around 95 GeV/c² at the CERN SPS Collider”, *Phys. Lett. B* **126** (1983) 398–410. [Cited on p. 8](#)
15. UA2 Collaboration, M. Banner *et al.*, “Observation of Single Isolated Electrons of High Transverse Momentum in Events with Missing Transverse Energy at the CERN anti-p p Collider”, *Phys. Lett. B* **122** (1983) 476–485. [Cited on p. 8](#)
16. J. A. Formaggio and G. P. Zeller, “From eV to EeV: Neutrino cross sections across energy scales”, *Rev. Mod. Phys.* **84** (Sep, 2012) 1307–1341. [Cited on pp. 8, 9, and 11](#)
17. P. Musset and J.-P. Vialle, “Neutrino physics with gargamelle”, *Physics Reports* **39** (1978) 1–130. [Cited on p. 11](#)
18. **Gargamelle Neutrino** Collaboration, F. J. Hasert *et al.*, “Observation of Neutrino Like Interactions without Muon or Electron in the Gargamelle Neutrino Experiment”, *Nucl. Phys. B* **73** (1974) 1–22. [Cited on p. 11](#)
19. F. J. Hasert *et al.*, “Search for Elastic ν_μ Electron Scattering”, *Phys. Lett. B* **46** (1973) 121–124. [Cited on p. 11](#)
20. M. Sajjad Athar, A. Fatima, and S. K. Singh, “Neutrinos and their interactions with matter”, *Prog. Part. Nucl. Phys.* **129** (2023) 104019, [arXiv:2206.13792 \[hep-ph\]](#). [Cited on p. 11](#)
21. K. Lande, L. M. Lederman, and W. Chinowsky, “Report on Long-Lived K⁰ Mesons”, *Phys. Rev.* **105** (Mar, 1957) 1925–1927. [Cited on p. 12](#)
22. B. Pontecorvo, “Mesonium and Antimesonium”, *Sov. Phys. JETP* **6** (1958) 429–431. [Cited on p. 12](#)
23. Z. Maki, M. Nakagawa, and S. Sakata, “Remarks on the unified model of elementary particles”, *Prog. Theor. Phys.* **28** (1962) 870–880. [Cited on p. 12](#)

24. A. Serenelli, "Alive and well: A short review about standard solar models", *The European Physical Journal A* **52** (Apr, 2016) 78. Cited on p. 13
25. J. N. Bahcall, W. F. Huebner, S. H. Lubow, P. D. Parker, and R. K. Ulrich, "Standard solar models and the uncertainties in predicted capture rates of solar neutrinos", *Rev. Mod. Phys.* **54** (Jul, 1982) 767–799. Cited on pp. 13 and 15
26. J. N. Bahcall, A. M. Serenelli, and S. Basu, "New solar opacities, abundances, helioseismology, and neutrino fluxes", *Astrophys. J. Lett.* **621** (2005) L85–L88, [arXiv:astro-ph/0412440](https://arxiv.org/abs/astro-ph/0412440). Cited on pp. 13 and 15
27. B. T. Cleveland, T. Daily, R. Davis, Jr., J. R. Distel, K. Lande, C. K. Lee, P. S. Widenhain, and J. Ullman, "Measurement of the solar electron neutrino flux with the Homestake chlorine detector", *Astrophys. J.* **496** (1998) 505–526. Cited on p. 13
28. **SAGE** Collaboration, J. N. Abdurashitov, *et al.*, "Measurement of the solar neutrino capture rate with gallium metal", *Phys. Rev. C* **60** (Oct, 1999) 055801. Cited on pp. 13, 14, and 22
29. W. Hampel, *et al.*, "GALLEX solar neutrino observations: results for GALLEX IV", *Physics Letters B* **447** (1999) 127–133. Cited on pp. 13 and 22
30. M. Altmann, *et al.*, "GNO solar neutrino observations: results for GNO I", *Physics Letters B* **490** (2000) 16–26. Cited on p. 13
31. **Super-Kamiokande** Collaboration, K. Abe, *et al.*, "Solar neutrino measurements in Super-Kamiokande-IV", *Phys. Rev. D* **94** (Sep, 2016) 052010. Cited on p. 14
32. **Kamiokande-II** Collaboration, K. S. Hirata *et al.*, "Experimental Study of the Atmospheric Neutrino Flux", *Phys. Lett. B* **205** (1988) 416. Cited on pp. 14 and 20
33. D. Casper, *et al.*, "Measurement of atmospheric neutrino composition with the IMB-3 detector", *Phys. Rev. Lett.* **66** (May, 1991) 2561–2564. Cited on p. 14
34. **The Super-Kamiokande** Collaboration, Y. Ashie, *et al.*, "Evidence for an Oscillatory Signature in Atmospheric Neutrino Oscillations", *Phys. Rev. Lett.* **93** (Sep, 2004) 101801. Cited on pp. 14 and 20
35. **OPERA** Collaboration, N. Agafonova, *et al.*, "Discovery of τ Neutrino Appearance in the CNGS Neutrino Beam with the OPERA Experiment", *Phys. Rev. Lett.* **115** (Sep, 2015) 121802. Cited on p. 14

36. **SNO** Collaboration, Q. R. Ahmad, *et al.*, “Measurement of the Rate of $\nu_e + d \rightarrow p + p + e^-$ Interactions Produced by 8B Solar Neutrinos at the Sudbury Neutrino Observatory”, *Phys. Rev. Lett.* **87** (Jul, 2001) 071301. *Cited on pp. 14 and 15*
37. **SNO** Collaboration, Q. R. Ahmad, *et al.*, “Direct Evidence for Neutrino Flavor Transformation from Neutral-Current Interactions in the Sudbury Neutrino Observatory”, *Phys. Rev. Lett.* **89** (Jun, 2002) 011301. *(Not cited.)*
38. **Super-Kamiokande** Collaboration, S. Fukuda, *et al.*, “Solar 8B and hep Neutrino Measurements from 1258 Days of Super-Kamiokande Data”, *Phys. Rev. Lett.* **86** (Jun, 2001) 5651–5655. *Cited on p. 15*
39. **SAGE** Collaboration, J. N. Abdurashitov, *et al.*, “Measurement of the solar neutrino capture rate with gallium metal. III. Results for the 2002–2007 data-taking period”, *Phys. Rev. C* **80** (Jul, 2009) 015807. *Cited on pp. 15 and 20*
40. **GNO** Collaboration, M. Altmann *et al.*, “Complete results for five years of GNO solar neutrino observations”, *Phys. Lett. B* **616** (2005) 174–190, [arXiv:hep-ex/0504037](https://arxiv.org/abs/hep-ex/0504037). *Cited on pp. 15 and 20*
41. **SNO** Collaboration, B. Aharmim, *et al.*, “Electron energy spectra, fluxes, and day-night asymmetries of 8B solar neutrinos from measurements with NaI dissolved in the heavy-water detector at the Sudbury neutrino observatory”, *Phys. Rev. C* **72** (Nov, 2005) 055502. *Cited on p. 15*
42. **Particle Data Group** Collaboration, S. Navas, *et al.*, “Review of particle physics”, *Phys. Rev. D* **110** (Aug, 2024) 030001. *Cited on pp. 16 and 18*
43. K. Zuber, *Neutrino Physics*. Series in High Energy Physics, Cosmology & Gravitation. Taylor & Francis, Boca Raton, FL, third edition. ed., 2020. *Cited on p. 17*
44. G. C. Branco, L. Lavoura, and M. N. Rebelo, “Majorana Neutrinos and CP Violation in the Leptonic Sector”, *Phys. Lett. B* **180** (1986) 264–268. *Cited on p. 18*
45. S. P. Mikheyev and A. Y. Smirnov, “Resonant amplification of neutrino oscillations in matter and solar neutrino spectroscopy”, *Nuovo Cim. C* **9** (1986) 17–26. *Cited on p. 18*
46. S. P. Mikheyev and A. Y. Smirnov, “Resonance Amplification of Oscillations in Matter and Spectroscopy of Solar Neutrinos”, *Sov. J. Nucl. Phys.* **42** (1985) 913–917. *(Not cited.)*

47. L. Wolfenstein, “Neutrino oscillations in matter”, *Phys. Rev. D* **17** (May, 1978) 2369–2374. Cited on p. 18
48. K. J. Kelly and S. J. Parke, “Matter density profile shape effects at DUNE”, *Phys. Rev. D* **98** (Jul, 2018) 015025. Cited on p. 18
49. O. Mena and S. Parke, “Unified graphical summary of neutrino mixing parameters”, *Phys. Rev. D* **69** (Jun, 2004) 117301. Cited on pp. 19 and 27
50. **Super-Kamiokande** Collaboration, K. Abe *et al.*, “Solar neutrino measurements using the full data period of Super-Kamiokande-IV”, *Phys. Rev. D* **109** (2024) 092001, [arXiv:2312.12907 \[hep-ex\]](https://arxiv.org/abs/2312.12907). Cited on p. 20
51. **Borexino** Collaboration, M. Agostini, *et al.*, “Experimental evidence of neutrinos produced in the CNO fusion cycle in the Sun”, *Nature* **587** (Nov, 2020) 577–582. Cited on p. 20
52. **KamLAND** Collaboration, A. Gando, *et al.*, “ ${}^7\text{Be}$ solar neutrino measurement with KamLAND”, *Phys. Rev. C* **92** (Nov, 2015) 055808. Cited on p. 20
53. **MACRO** Collaboration, M. Ambrosio *et al.*, “Matter effects in upward going muons and sterile neutrino oscillations”, *Phys. Lett. B* **517** (2001) 59–66, [arXiv:hep-ex/0106049](https://arxiv.org/abs/hep-ex/0106049). Cited on p. 20
54. **T2K** Collaboration, K. Abe, *et al.*, “Observation of Electron Neutrino Appearance in a Muon Neutrino Beam”, *Phys. Rev. Lett.* **112** (Feb, 2014) 061802. Cited on p. 21
55. **T2K** Collaboration, K. Abe *et al.*, “Measurements of neutrino oscillation parameters from the T2K experiment using 3.6×10^{21} protons on target”, *Eur. Phys. J. C* **83** (2023) 782, [arXiv:2303.03222 \[hep-ex\]](https://arxiv.org/abs/2303.03222). Cited on p. 21
56. **NOvA** Collaboration, P. Adamson, *et al.*, “Constraints on Oscillation Parameters from ν_e Appearance and ν_μ Disappearance in NOvA”, *Phys. Rev. Lett.* **118** (Jun, 2017) 231801. Cited on p. 21
57. **KamLAND** Collaboration, K. Eguchi, *et al.*, “First Results from KamLAND: Evidence for Reactor Antineutrino Disappearance”, *Phys. Rev. Lett.* **90** (Jan, 2003) 021802. Cited on p. 21
58. **Double Chooz** Collaboration, Y. Abe, *et al.*, “Indication of Reactor $\bar{\nu}_e$ Disappearance in the Double Chooz Experiment”, *Phys. Rev. Lett.* **108** (Mar, 2012) 131801. Cited on p. 21

59. F. P. An, *et al.*, “Observation of Electron-Antineutrino Disappearance at Daya Bay”, *Phys. Rev. Lett.* **108** (Apr, 2012) 171803. [Cited on p. 21](#)
60. **RENO** Collaboration, J. K. Ahn, *et al.*, “Observation of Reactor Electron Antineutrinos Disappearance in the RENO Experiment”, *Phys. Rev. Lett.* **108** (May, 2012) 191802. [Cited on p. 21](#)
61. M. A. Acero *et al.*, “White paper on light sterile neutrino searches and related phenomenology”, *J. Phys. G* **51** (2024) 120501, [arXiv:2203.07323 \[hep-ex\]](#). [Cited on p. 22](#)
62. **LSND Collaboration** Collaboration, A. Aguilar, *et al.*, “Evidence for neutrino oscillations from the observation of $\bar{\nu}_e$ appearance in a $\bar{\nu}_\mu$ beam”, *Phys. Rev. D* **64** (Nov, 2001) 112007. [Cited on pp. 22, 23, and 24](#)
63. **MiniBooNE** Collaboration, A. A. Aguilar-Arevalo *et al.*, “A Combined $\nu_\mu \rightarrow \nu_e$ and $\bar{\nu}_\mu \rightarrow \bar{\nu}_e$ Oscillation Analysis of the MiniBooNE Excesses”, 7, 2012. [arXiv:1207.4809 \[hep-ex\]](#). [Cited on p. 22](#)
64. G. Mention, M. Fechner, T. Lasserre, T. A. Mueller, D. Lhuillier, M. Cribier, and A. Letourneau, “The Reactor Antineutrino Anomaly”, *Phys. Rev. D* **83** (2011) 073006, [arXiv:1101.2755 \[hep-ex\]](#). [Cited on pp. 22 and 24](#)
65. S. R. Elliott, V. Gavrin, and W. Haxton, “The gallium anomaly”, *Prog. Part. Nucl. Phys.* **134** (2024) 104082, [arXiv:2306.03299 \[nucl-ex\]](#). [Cited on p. 22](#)
66. **KARMEN** Collaboration, B. Armbruster, *et al.*, “Upper limits for neutrino oscillations $\bar{\nu}_\mu \rightarrow \bar{\nu}_e$ from muon decay at rest”, *Phys. Rev. D* **65** (Jun, 2002) 112001. [Cited on pp. 23 and 28](#)
67. B. Louis, V. Sandberg, H. White, and D. Kestenbaum, “A thousand eyes: The story of LSND”, *Los Alamos Science* (1997) 92–115. [Cited on p. 24](#)
68. **MiniBooNE** Collaboration, A. A. Aguilar-Arevalo *et al.*, “Updated MiniBooNE neutrino oscillation results with increased data and new background studies”, *Phys. Rev. D* **103** (2021) 052002, [arXiv:2006.16883 \[hep-ex\]](#). [Cited on p. 24](#)
69. C. Giunti, Y. F. Li, C. A. Ternes, O. Tyagi, and Z. Xin, “Gallium Anomaly: critical view from the global picture of ν_e and $\bar{\nu}_e$ disappearance”, *JHEP* **10** (2022) 164, [arXiv:2209.00916 \[hep-ph\]](#). [Cited on pp. 25 and 29](#)
70. **NOMAD** Collaboration, P. Astier *et al.*, “Search for $\nu_\mu \rightarrow \nu_e$ oscillations in the NOMAD experiment”, *Phys. Lett. B* **570** (2003) 19–31, [arXiv:hep-ex/0306037](#). [Cited on p. 28](#)

71. C. Rubbia, "The Liquid Argon Time Projection Chamber: A New Concept for Neutrino Detectors", Tech. Rep. CERN-EP-INT-77-08, CERN-EP-77-08, CERN, 5, 1977. [Cited on pp. 28, 33, and 40](#)
72. MicroBooNE Collaboration, P. Abratenko, *et al.*, "Search for an excess of electron neutrino interactions in MicroBooNE using multiple final-state topologies", *Phys. Rev. Lett.* **128** (Jun, 2022) 241801. [Cited on p. 28](#)
73. C. A. Argüelles, I. Esteban, M. Hostert, K. J. Kelly, J. Kopp, P. A. N. Machado, I. Martinez-Soler, and Y. F. Perez-Gonzalez, "MicroBooNE and the ν_e Interpretation of the MiniBooNE Low-Energy Excess", *Phys. Rev. Lett.* **128** (Jun, 2022) 241802. [Cited on p. 28](#)
74. ICARUS Collaboration, M. Antonello *et al.*, "Search for anomalies in the ν_e appearance from a ν_μ beam", *Eur. Phys. J. C* **73** (2013) 2599, [arXiv:1307.4699 \[hep-ex\]](#). [Cited on pp. 28 and 46](#)
75. M. Antonello *et al.*, "Some conclusive considerations on the comparison of the ICARUS $\nu_\mu \rightarrow \nu_e$ oscillation search with the MiniBooNE low-energy event excess", [arXiv:1502.04833 \[hep-ph\]](#). [Cited on p. 28](#)
76. OPERA Collaboration, N. Agafonova *et al.*, "New results on $\nu_\mu \rightarrow \nu_\tau$ appearance with the OPERA experiment in the CNGS beam", *JHEP* **11** (2013) 036, [arXiv:1308.2553 \[hep-ex\]](#). [Erratum: JHEP 04, 014 (2014)]. [Cited on pp. 28 and 46](#)
77. Y. Declais *et al.*, "Search for neutrino oscillations at 15-meters, 40-meters, and 95-meters from a nuclear power reactor at Bugey", *Nucl. Phys. B* **434** (1995) 503–534. [Cited on p. 28](#)
78. NEOS Collaboration, Y. J. Ko, *et al.*, "Sterile neutrino search at the NEOS experiment", *Phys. Rev. Lett.* **118** (Mar, 2017) 121802. [Cited on p. 28](#)
79. PROSPECT Collaboration, M. Andriamirado *et al.*, "Improved short-baseline neutrino oscillation search and energy spectrum measurement with the PROSPECT experiment at HFIR", *Phys. Rev. D* **103** (2021) 032001, [arXiv:2006.11210 \[hep-ex\]](#). [Cited on p. 28](#)
80. STEREO Collaboration, H. Almazán *et al.*, "STEREO neutrino spectrum of ^{235}U fission rejects sterile neutrino hypothesis", *Nature* **613** (2023) 257–261, [arXiv:2210.07664 \[hep-ex\]](#). [Cited on p. 28](#)

81. **RENO and NEOS** Collaboration, Z. Atif, *et al.*, “Search for sterile neutrino oscillations using RENO and NEOS data”, *Phys. Rev. D* **105** (Jun, 2022) L111101. [Cited on p. 29](#)
82. M. Maltoni, “(eV) sterile neutrinos: Global picture and local views”, in *XXXI International Conference on Neutrino Physics and Astrophysics*. Milan, Italy, June, 2024. <https://agenda.infn.it/event/37867/contributions/233957>. [Cited on p. 29](#)
83. A. P. Serebrov, R. M. Samoilov, M. E. Chaikovskii, and O. M. Zhrebtssov, “The result of the Neutrino-4 experiment, sterile neutrinos and dark matter, the fourth neutrino and the Hubble constant”, [arXiv:2302.09958 \[hep-ph\]](https://arxiv.org/abs/2302.09958). [Cited on p. 29](#)
84. **NOvA** Collaboration, P. Adamson *et al.*, “Search for active-sterile neutrino mixing using neutral-current interactions in NOvA”, *Phys. Rev. D* **96** (2017) 072006, [arXiv:1706.04592 \[hep-ex\]](https://arxiv.org/abs/1706.04592). [Cited on p. 29](#)
85. **MINOS+** Collaboration, P. Adamson *et al.*, “Search for sterile neutrinos in MINOS and MINOS+ using a two-detector fit”, *Phys. Rev. Lett.* **122** (2019) 091803, [arXiv:1710.06488 \[hep-ex\]](https://arxiv.org/abs/1710.06488). [Cited on p. 29](#)
86. M. Dentler, Á. Hernández-Cabezudo, J. Kopp, P. A. N. Machado, M. Maltoni, I. Martínez-Soler, and T. Schwetz, “Updated Global Analysis of Neutrino Oscillations in the Presence of eV-Scale Sterile Neutrinos”, *JHEP* **08** (2018) 010, [arXiv:1803.10661 \[hep-ph\]](https://arxiv.org/abs/1803.10661). [Cited on pp. 29 and 30](#)
87. **ICARUS-WA104, LAr1-ND, MicroBooNE** Collaboration, C. Rubbia, “A Proposal for a Three Detector Short-Baseline Neutrino Oscillation Program in the Fermilab Booster Neutrino Beam”, Tech. Rep. FERMILAB-LOI-2015-01, 1, 2015. [arXiv:1503.01520 \[physics.ins-det\]](https://arxiv.org/abs/1503.01520). [Cited on pp. 29, 33, 35, 37, and 38](#)
88. A. Diaz, C. A. Argüelles, G. H. Collin, J. M. Conrad, and M. H. Shaevitz, “Where Are We With Light Sterile Neutrinos?”, *Phys. Rept.* **884** (2020) 1–59, [arXiv:1906.00045 \[hep-ex\]](https://arxiv.org/abs/1906.00045). [Cited on p. 31](#)
89. S. Böser, C. Buck, C. Giunti, J. Lesgourgues, L. Ludhova, S. Mertens, A. Schukraft, and M. Wurm, “Status of Light Sterile Neutrino Searches”, *Prog. Part. Nucl. Phys.* **111** (2020) 103736, [arXiv:1906.01739 \[hep-ex\]](https://arxiv.org/abs/1906.01739). [Cited on p. 31](#)
90. R. Triozzi, A. Guglielmi, and D. Gibin, *Study of the Trigger System Performance of the ICARUS T600 Detector at Fermilab Exposed to the Booster and NuMI Neutrino*

- Beams*. M. Sc. thesis, Università degli studi di Padova, Padova, 2023. [Cited on p. 40](#)
91. M. Artero Pons, D. Gibin, and G. Monaco, *Study of the Reconstruction of ν_μ CC QE Events from the Booster Neutrino Beam with the ICARUS Detector*. PhD thesis, Università degli studi di Padova, Padova, 2023. [Cited on pp. 54 and 60](#)
 92. P. A. Machado, O. Palamara, and D. W. Schmitz, “The Short-Baseline Neutrino Program at Fermilab”, *Ann. Rev. Nucl. Part. Sci.* **69** (2019) 363–387, [arXiv:1903.04608 \[hep-ex\]](#). [Cited on pp. 33, 34, and 37](#)
 93. **ICARUS** Collaboration, F. Abd Alrahman, *et al.*, “Search for a Hidden Sector Scalar from Kaon Decay in the Dimuon Final State at ICARUS”, *Phys. Rev. Lett.* **134** (Apr, 2025) 151801. [Cited on pp. 37 and 39](#)
 94. R. Ainsworth, P. Adamson, B. C. Brown, D. Capista, K. Hazelwood, I. Kourbanis, D. K. Morris, M. Xiao, and M.-J. Yang, “High intensity operation using proton stacking in the fermilab recycler to deliver 700 kw of 120 gev proton beam”, *Phys. Rev. Accel. Beams* **23** (Dec, 2020) 121002. [Cited on p. 37](#)
 95. **MiniBooNE** Collaboration, A. A. Aguilar-Arevalo, *et al.*, “Neutrino flux prediction at MiniBooNE”, *Phys. Rev. D* **79** (Apr, 2009) 072002. [Cited on pp. 38 and 39](#)
 96. J. N. Marx and D. R. Nygren, “The Time Projection Chamber”, *Phys. Today* **31N10** (1978) 46–53. [Cited on p. 40](#)
 97. **ALICE** Collaboration, C. Lippmann, “Upgrade of the ALICE Time Projection Chamber”, Tech. Rep. CERN-LHCC-2013-020, ALICE-TDR-016, 3, 2014. [Cited on p. 40](#)
 98. **SBND** Collaboration, R. Acciarri *et al.*, “The Short-Baseline Near Detector at Fermilab: Input to the European Strategy for Particle Physics 2026 Update”, Tech. Rep. FERMILAB-PUB-25-0154-PPD, 3, 2025. [arXiv:2504.00245 \[hep-ex\]](#). [Cited on p. 43](#)
 99. **ICARUS** Collaboration, S. Amerio *et al.*, “Design, construction and tests of the ICARUS T600 detector”, *Nucl. Instrum. Meth. A* **527** (2004) 329–410. [Cited on pp. 45 and 46](#)
 100. **ICARUS** Collaboration, P. Abratenko *et al.*, “ICARUS at the Fermilab Short-Baseline Neutrino program: initial operation”, *Eur. Phys. J. C* **83** (2023) 467, [arXiv:2301.08634 \[hep-ex\]](#). [Cited on pp. 46 and 48](#)

101. M. Antonello *et al.*, “Experimental observation of an extremely high electron lifetime with the ICARUS-T600 LAr-TPC”, *JINST* **9** (2014) P12006, [arXiv:1409.5592 \[physics.ins-det\]](https://arxiv.org/abs/1409.5592). Cited on p. 46
102. **ICARUS-T600** Collaboration, L. Bagby *et al.*, “Overhaul and Installation of the ICARUS-T600 Liquid Argon TPC Electronics for the FNAL Short Baseline Neutrino Program”, *JINST* **16** (2021) P01037, [arXiv:2010.02042 \[physics.ins-det\]](https://arxiv.org/abs/2010.02042). Cited on p. 48
103. **ICARUS** Collaboration, F. A. Alrahman *et al.*, “Operation of the Trigger System for the ICARUS Detector at Fermilab”, [arXiv:2506.20137 \[hep-ex\]](https://arxiv.org/abs/2506.20137). Cited on p. 52
104. K. Biery, C. Green, J. Kowalkowski, M. Paterno, and R. Rechenmacher, “artdaq: An Event-Building, Filtering, and Processing Framework”, *IEEE Trans. Nucl. Sci.* **60** (2013) 3764 – 3771. Cited on p. 52
105. C. Green, J. Kowalkowski, M. Paterno, M. Fischler, L. Garren, and Q. Lu, “The Art Framework”, *J. Phys. Conf. Ser.* **396** (2012) 022020. Cited on p. 53
106. **ICARUS** Collaboration, A. Aduszkiewicz *et al.*, “Design and implementation of the cosmic ray tagger system for the ICARUS detector at FNAL”, *JINST* **20** (2025) T04002, [arXiv:2501.03034 \[hep-ex\]](https://arxiv.org/abs/2501.03034). Cited on p. 54
107. F. Poppi, *The cosmic ray tagger of the ICARUS detector: construction, commissioning and performances in the first physics run*. PhD thesis, amsdottorato, Alma Mater Studiorum - Università di Bologna, Bologna U., 2023. Cited on p. 60
108. **ICARUS** Collaboration, F. Poppi, “The Cosmic Ray Tagger system of the ICARUS detector at Fermilab”, *PoS ICHEP2022* (2022) 580. Cited on p. 54
109. E. D. Church, “LArSoft: A Software Package for Liquid Argon Time Projection Drift Chambers”, [arXiv:1311.6774 \[physics.ins-det\]](https://arxiv.org/abs/1311.6774). Cited on p. 54
110. E. L. Snider and G. Petrillo, “LArSoft: Toolkit for Simulation, Reconstruction and Analysis of Liquid Argon TPC Neutrino Detectors”, *J. Phys. Conf. Ser.* **898** (2017) 042057. (Not cited.)
111. R. Pordes and E. Snider, “The Liquid Argon Software Toolkit (LArSoft): Goals, Status and Plan”, in *Proceedings of 38th International Conference on High Energy Physics — PoS(ICHEP2016)*, vol. 282, p. 182. 2017. Cited on p. 54

112. R. Brun, *et al.*, “root-project/root: v6.18/02”, Aug., 2019. [Cited on p. 56](#)
113. **ICARUS** Collaboration, P. Abratenko *et al.*, “Calibration and simulation of ionization signal and electronics noise in the ICARUS liquid argon time projection chamber”, *JINST* **20** (2025) P01032, [arXiv:2407.11925 \[hep-ex\]](#).
[Cited on p. 57](#)
114. **MicroBooNE** Collaboration, C. Adams *et al.*, “Ionization electron signal processing in single phase LArTPCs. Part I. Algorithm Description and quantitative evaluation with MicroBooNE simulation”, *JINST* **13** (2018) P07006, [arXiv:1802.08709 \[physics.ins-det\]](#). [Cited on p. 58](#)
115. **MicroBooNE** Collaboration, C. Adams *et al.*, “Ionization electron signal processing in single phase LArTPCs. Part II. Data/simulation comparison and performance in MicroBooNE”, *JINST* **13** (2018) P07007, [arXiv:1804.02583 \[physics.ins-det\]](#). [Cited on p. 58](#)